MASTER'S DISSERTATION

Interplay between magnetic fields, convection and radiation: The brightness of the stellar faculae

Helena Vila Crespo

Academic course: 2023-24
Supervisors: Nikola Vitas & Elena Khomenko

July, 2nd 2024

Resumen:

El Sol, una estrella de secuencia principal G2V, sirve de modelo representativo para todas las estrellas frías de secuencia principal, que comparten una estructura global común influida por los campos magnéticos, que desempeñan un papel crucial en diversos fenómenos estelares. En este trabajo se revisa y amplía el modelo de Spruit, que reproduce con exactitud las intensidades relativas observadas en la superficie solar, incorporando consideraciones termodinámicas y campos magnéticos. A pesar de su simplicidad, el modelo de Spruit proporciona una visión significativa de los mecanismos físicos que subyacen a estas observaciones y facilita la parametrización de los modelos de los tubos de flujo, que son esenciales para para comprender la actividad magnética estelar.

Por el contrario, las simulaciones realistas tridimensionales, si bien son exhaustivas y tienen en cuenta una amplia gama de procesos físicos, a menudo ocultan los mecanismos de la actividad magnética estelar. Este trabajo pretende clarificar los detalles y métodos del modelo de Spruit reimplementándolo con métodos numéricos modernos para analizar su dependencia de parámetros específicos de diferentes tipos estelares y composiciones. La metodología implica un estudio detallado del método de Spruit, la introducción de esquemas numéricos avanzados, seguido de un estudio en profundidad de la transferencia radiativa. Nuestra implementación actualizada amplía significativamente la aplicabilidad del modelo de Spruit a otras estrellas, proporcionando una contrapartida semianalítica a simulaciones complejas. Este modelo mejorado permite una comprensión más profunda de cómo influyen los distintos parámetros en el comportamiento de los tubos de flujo magnético en diferentes entornos estelares. Los resultados se comparan minuciosamente con los resultados originales de Spruit, destacando tanto las similitudes como las diferencias. También analizamos cómo los parámetros que definen el tubo de flujo afectan a sus propiedades y la distribución de la temperatura, proporcionando nuevos conocimientos sobre la dinámica magnética estelar.

Este trabajo no sólo valida los aspectos fundamentales del modelo de Spruit, sino que amplía su alcance.

Abstract:

The Sun, a G2V main sequence star, serves as a representative model for all cool main sequence stars, sharing a common global structure influenced by magnetic fields, which play a crucial role in various stellar phenomena. This dissertation revisits and extends Spruit's model, which accurately reproduces observed relative intensities at the solar surface by incorporating thermodynamic considerations and magnetic fields. Despite its simplicity, Spruit's model provides significant insights into the physical mechanisms behind these observations and facilitates the parameterisation of flux tube models, which are essential for understanding stellar magnetic activity.

In contrast, three-dimensional realistic simulations, while comprehensive in accounting for a wide range of physical processes, often obscure the underlying mechanisms due to their complexity. This work aims to clarify the details and methods behind Spruit's model by re-implementing it using modern numerical methods to analyse its dependence on parameters specific to different stellar types and chemical compositions. The methodology involves a detailed study of Spruit's setup, the introduction of advanced numerical schemes, followed by an in-depth study of radiative transfer.

Our updated implementation significantly extends the applicability of Spruit's model to other stars, providing a semi-analytical counterpart to complex simulations. This improved model allows a deeper understanding of how different parameters influence the behaviour of magnetic flux tubes in different stellar environments. The results are carefully compared with Spruit's original findings, highlighting both similarities and differences. We also analyse how the parameters defining the flux tube affect its properties and temperature distribution, providing new insights into stellar magnetic dynamics.

This work not only validates the fundamental aspects of Spruit's model, but also extends its scope.

Contents

1 Introduction

The Sun is our nearest star. It is the only star in the universe which surface is resolvable in direct observations. By its global parameters (effective temperature, surface gravity acceleration), it is a main sequence (MS) star of the G2V class, so called a yellow dwarf. It may be taken as a typical representative of all cool main sequence stars (stellar classes F, G, K and M). Although there are some important differences among the cool stars, their global structure is similar. They all have a small core where the nuclear reactions take place, which is enveloped by shells or zones where, moving outward, the energy is dominantly transferred by radiation or by convection. The radial extent of these zones may significantly vary between the classes. Finally, they all have relatively thin atmospheres which can roughly be divided into photospheres where the mean temperature and density drop with height and the chromospheres where the density keeps decreasing with height, but the temperature increases due to complex interactions between radiation and magnetized plasma which are not yet fully understood (Carlsson et al., 2019).

The magnetic fields are ubiquitous for the cool stars. Stellar magnetic fields may be generated either through the action of the global dynamo owing to the differential rotation in the stellar interiors, or they may be amplified by the action of the small-scale dynamo that operates in the turbulent convection (Vögler and Schüssler, 2007; Perdomo García et al., 2023).

In the magnetohydrodynamic (MHD) approximation, the plasma is constrained from crossing the magnetic field lines. As the magnetic fields penetrate the near-surface convection zone, they significantly influence local plasma dynamics. This alteration results in a reduction in convective energy transport, which subsequently causes a localized drop in emergent intensity at the stellar surface (Biermann, 1941). Consequently, in the Sun, these alterations in local brightness give rise to a number of phenomena collectively nicknamed "solar dermatology" (Cameron, 2009) including sunspots, pores, and small magnetic elements.

The presence of magnetic field is intricately linked to all aspects of solar activity. Magnetographic (spectroscopic and spectropolarimetric) methods offer valuable insights into distribution of the field at the photospheric level, revealing the existence of magnetic flux tubes. The majority of these tubes are notably small, with radii of the order of a few hundreds of kilometers. These magnetic fields in the solar interior and lower solar atmosphere are concentrated into discrete structures, which are characterised by strong magnetic fields and are surrounded by a relatively field-free plasma. Although magnetic flux concentrations are inherently asymmetric in reality, for the purposes of analytical or semi-analytical magnetohydrostatic modelling, they can be approximated as axially symmetric tubes (see Solanki, 1993). Faculae[1] are generally bright relative to the quiet solar surface towards the limb, but have low contrast at most wavelengths at the centre of the disc (Spruit, 1976). They are identified on conglomerates of smaller magnetic elements. Due to the constant interplay between the magnetic flux and the convective motions in the atmosphere, the concentrations of the magnetic field, seen on the surface as spots, faculae and network, evolve in time.

Simple physical models are useful for understanding the nature of individual physical processes; by neglecting many of the physical interactions present, it is possible to isolate processes of particular interest and study them in detail.

1.1 Spruit's model in a nutshell

Spruit (1976), constructed numerical models of flux tubes making various assumptions regarding the geometry of a tube, heat transfer inside and outside of a tube, and distribution of its magnetic

[1] Singular *facula* is borrowed from Latin, meaning a "little torch".

field. The goal of this pioneering work was to explain the observed brightness of magnetic elements of different size and at different positions at the solar disk. The resulting model is characterized by an infinitely thin current sheet at the interface between the field and the field-free external plasma.

The darkness of sunspots suggests a significant reduction in non-radiative energy transport, a phenomenon that underscores the interplay between radiation and magnetic fields in solar phenomena. This interaction becomes particularly pronounced in the lateral influx of radiation, which plays a crucial role in determining the appearance of flux tubes. It is remarkable that the radius of the tube strongly influences its features. In the thinnest flux fibres, the lateral radiation field creates a warm bottom, which causes the interior of the tube to be warmer than the photosphere outside the tube at the same optical depth. However, at the same geometrical depth, the tube's interior is cooler than the convective zone outside. In white light observations, the brightest part of the flux tube is its cylindrical bright wall, which is best observed when looking towards the solar limb. Near the centre of the solar disk, micropores can be distinguished as features between truly dark pores and bright faculae, revealing a relatively dark bottom surrounded by a bright wall. This detailed understanding, encapsulated in Spruit's thin tube approximation model, has been demonstrated to fairly represent observations, particularly the transition case between bright magnetic element and dark pore.

In his model, Spruit introduced several simplifications. He assumed that plasma is in magnetohydrostatic equilibrium, that both radiative and convective transport can be described as diffusion processes, and that the current sheet is infinitesimally thin. The original paper is divided in three distinctive parts. Initial models (his Sect. 1) are in hydrostatic balance and satisfy the energy balance equation. The free parameters are the radius of the tube (r_0), its Wilson depression (z_w) and the parameter q specifying the efficiency of the vertical convective heat transport within the tube. Then the potential magnetic field is added keeping the thermal structure unchanged (Sect. 2), and, finally, the formation of the emergent radiation is computed and discussed (Sect. 3). We have to underline that the magnetic elements in these models are superposed on an already relaxed thermal structure, i.e. they are not formed through dynamical interaction with the velocity fields and with the thermodynamic state of plasma. In his point (vii), Spruit acknowledges that the models produced in Sect. 1, before explicitly adding any magnetic field, are already capable of giving reasonable estimate of the emergent intensity. This is an extremely important point as it allows to study and analyze the brightness of magnetic structures in other stars without going into the complex modeling of the magnetic field itself, but rather by varying the input parameters r_0, z_w and q.

While these approximations provided valuable insights, they were gradually relaxed in more recent investigations of magnetic flux concentrations. Some the subsequent work focused on finding better representation of the magnetic field structure of the tube including its third spatial component assuming that the atmosphere has horizontally homogeneous temperature (for example Pizzo (1986, 1993); Khomenko and Collados (2008)), and some focused on the solution of both the pressure, energy and the magnetic equilibrium together in early magnetohydrodynamic codes (see Deinzer et al., 1984) which finally led to state-of-the-art three-dimensional realistic numerical simulations (Vögler, Shelyag, et al., 2005 and Norris, Beeck, et al., 2017). A comprehensive summary of the progress in modelling flux tubes can be found in reviews by Solanki (1993) and Stenflo (1989), as well as in the book by Schrijver (2008).

These models have led to a better description of the warm bottom around $\tau \sim 1$, where τ stands for the optical depth. In addition, both steady and dynamic models indicate a narrow downflow region just outside the magnetopause. This convective downflow is triggered by the

increased radiative cooling through the flux tube, which is more transparent than its surroundings. This leads to a symbiosis between the flux tubes and the thin convective downdrafts, which is fundamental to the interplay between convection and the magnetic field.

1.2 Dark faculae: Norris et al

One-dimensional models are effective in capturing the overall disk-integrated properties of faculae. However, they fail to reproduce observed limb-dependent contrasts due to their inability to account for the geometric effects of neighbouring granules and the evacuation of the magnetic feature. Three-dimensional simulations, however, can provide more realistic centre-to-limb variations (CLV) for facular contrasts by incorporating the mix of atmospheric features present along the line of sight when viewing faculae towards the limb. Afram et al. (2011) modelled the centre-to-limb variation of contrast for these features on the Sun in three dimensions, but only for a single wavelength band. Norris et al. (2017) further developed this approach by presenting synthetic spectra from ultraviolet (UV) to far infrared (FIR), derived from three-dimensional magneto-convection simulations of a Sun-like stellar photosphere with spectral type G2 and a gravitational acceleration of $\log g \approx 4.44$. In order to achieve their objectives, they used the magnetohydrodynamics (MHD) code MURaM (Vögler, Shelyag, et al., 2005), which incorporates an array of average magnetic fields ranging from 0 to 500 G.

In a subsequent study, Norris et al. (2023) conducted magnetoconvection simulations for K0, M0, and M2 main-sequence stars with varying injected vertical magnetic fields. This study yielded unexpected results. They predicted that for early M stars with a magnetic field of 300 G, features typically brighter than the quiet Sun would appear darker, except near the limb and in the UV. Furthermore, the G2 simulations can be used as a preliminary indicator of the contrasts expected in late-F stars.[2]

1.3 The aim of this work

As we saw, Spruit's model is capable of reproducing the observed relative intensities at the solar surfaces already from thermodynamic considerations and with surprising accuracy. This model is remarkably simple, but extremely powerful as it allows an insight into the physical mechanism behind the observed intensities, and it allows the models of fluxtubes to be parametrized. On the other egde of the complexity spectrum, the realistic simulations by Norris et al. are comprehensive in terms of physical process that they account for. When applied to cool stars, they reveal behaviour opposite to that that Spruit's model predicted for the sun. Although the realistic simulations provide results that can accurately reproduce detailed observations, the complexity of these computations and the highly non-linear time-dependent solutions often limit (obscure) the understanding of the processes involved.

However, the simplicity of Spruit's model does not mean that it is entirely trivial to reproduce. The original paper does not reveal all the details of the numerical methods used in the computation, neither it discusses the effects that some of the assumptions have on the resulting models. One of the motivations of this thesis is to understand the hidden details and the method behind this model.

[2]Note that all results in Norris et. al paper assume solar metallicity.

In this thesis we revisit Spruit's model, study its details and implement it in terms of modern numerical methods. The aim is to analyze the dependency of this method on parameters that are specific to a certain star (stellar type and chemical composition). In this way, the newly developed numerical implementation of Spruit's original work is applicable to other stars. Moreover, this work should provide a semi-analytical counterpart to the study of Norris at al. and help understanding the mechanism why the brightness of the stellar faculae vary with effective temperature and surface gravity.

2 Methodology: Spruit's model

To describe plasma, we use the magnetohydrodynamics (MHD) equations. In their conservative form, these are written as:

$$\frac{\partial \rho}{\partial t} + \nabla(\rho \mathbf{v}) = 0 \tag{1a}$$

$$\frac{\partial \rho \mathbf{v}}{\partial t} + \nabla \left[\rho \mathbf{v}\mathbf{v} + \left(p + \frac{\mathbf{B}^2}{2\mu_0} \right) \mathbf{I} - \frac{\mathbf{B}\mathbf{B}}{\mu_0} \right] = \rho \mathbf{g} \tag{1b}$$

$$\frac{\partial e}{\partial t} + \nabla \left[\mathbf{v} \left(e + p + \frac{\mathbf{B}^2}{2\mu_0} \right) - \frac{\mathbf{B}(\mathbf{v}\mathbf{B})}{\mu_0} \right] = \rho(\mathbf{g}\mathbf{v}) + Q_{rad} \tag{1c}$$

$$\frac{\partial \mathbf{B}}{\partial t} = \nabla \times (\mathbf{v} \times \mathbf{B}) \tag{1d}$$

which are, respectively, the mass, the momentum and the energy conservation laws, and the induction equation. The magnitudes involved are: the mass density ρ, the velocity v, the pressure p, the magnetic field $\mathbf{B}$, the vacuum magnetic permeability μ_0, the gravity acceleration $\mathbf{g}$, the internal energy e and the radiative energy exchange term Q_{rad}. The system is closed by the equation of state, and by the radiative transfer equation accounting for the interaction between light and matter. In our approach we assume a situation of hydrostatic equilibrium. In hydrostatic equilibrium, all forces are balanced, resulting in a net force of zero. Consequently, the velocity of the fluid is zero, which allows us to omit any terms involving velocity from our equations. Furthermore, as we are dealing with a hydrodynamic situation where magnetic fields are negligible, the induction equation becomes redundant and is therefore not considered in our analysis. The system of equations above is thus reduced to:

$$\nabla p = \rho \mathbf{g} \tag{2a}$$

$$\text{const} = Q_{conv} + Q_{rad} \tag{2b}$$

where Q_{conv} stands for the convective flux. In the first equation we recognized the equation of hydrostatic equilibrium (in one-dimensional problems, when the vertical geometrical axis is labeled by z, ∇ becomes $\mathrm{d}/\mathrm{d}z$), and, in the second, we recognized the equation of the energy balance. If we strictly derive the Eq. (1c), the result is $Q_{rad} = 0$. However, we need to consider the radiative and conductive fluxes to get a more complete picture of the energy balance, where "const" stands for a cooling term.

The system is further closed by the equation of state and the radiative transfer equation, while the convective energy flux is solved using mixing length theory (MLT, see Stix, 2004).

One of the key assumptions in Spruit's model is that both radiative transfer and convection in Eq. (2b) are calculated as diffusion processes. This assumption leads to a steady-state diffusion approximation. In the steady state, the energy equation typically balances the divergence of

conductive and radiative heat fluxes, "const" is set equal to zero as we don't consider any additional internal heat sources:

$$\nabla(Q_{conv} + Q_{rad}) = 0 \tag{3}$$

For the diffusion approximation, the radiative and convective fluxes can be written as $Q_{conv} = k_0 \nabla T$ and $Q_{rad} = k_1 \nabla T$, so $Q_{conv} + Q_{rad} = K \nabla T$. These assumptions result in the temperature satisfying:

$$\nabla \cdot (K \nabla T) = 0 \tag{4}$$

where K is the diffusion coefficient that accounts for both radiative and convective energy transport. K is allowed to be anisotropic and depth dependent, it is taken different inside and outside the tube, and is not dependent on the horizontal direction.

2.1 The flux tube setup

Spruit's *thin-tube approximation* assumes that the width of a flux tube is small compared to the scale of the vertical stratification given by the pressure scale height H_p.

In this model, it is assumed a hydrostatic equilibrium (HSE) situation. The tubes can be characterised by three basic input parameters: the radius, the Wilson depression, and the heat flux. These tubes are treated as magnetic elements and we make the following specific assumptions about their properties:

- The energy transport is described by diffusion with a depth-dependent anisotropic diffusion coefficient. This coefficient varies with depth, but is reduced inside the tube compared to the outside, while maintaining a similar depth dependence.
- There is no convective transport across the magnetic field lines. This means that the convective diffusion coefficient inside the tube is lower than outside, reflecting the inhibition of convective motions by the presence of the magnetic field.
- The magnetic field inside the tube must satisfy pressure equilibrium. This ensures that the magnetic pressure and the gas pressure inside the tube balance the external pressure.

By incorporating these assumptions, we model the tube as a magnetic element in the context of hydrostatic equilibrium. From the observational data we note that faculae near the centre of the solar disc have low contrast. This observation allows us to approximate the temperature inside the flux tube in the Wilson depression ($T_{in}(z_w)$) to be roughly equal to the temperature of the quiet Sun at the surface ($T_{out}(0)$). This approximation suggests that $T_{in}(z_w) \approx T_{out}(0)$. Consequently, the observable layers of the magnetic structure in the flux tube, which have the temperature $T_{in}(z_w)$, resemble the structure of the unperturbed photosphere/upper convection zone, but are shifted downwards by the Wilson depression (z_w). This downward shift indicates that the observable layers of the flux tube are at a lower geometric height compared to the quiet solar photosphere. In summary, even under hydrostatic equilibrium conditions, the flux tube is assumed to maintain the characteristics of a magnetic element. This includes specific energy transport and pressure equilibrium properties.

In the following section we use this approximation to estimate the relation between the interior and the exterior diffusion coefficients. The shift of the model with respect to the photospheric model implies that the interior is cool relative to its surroundings. A schema of the model is shown in Fig. 1, we to the surface at the point where $z = 0$ and the vertical axis is counted positively inwards.

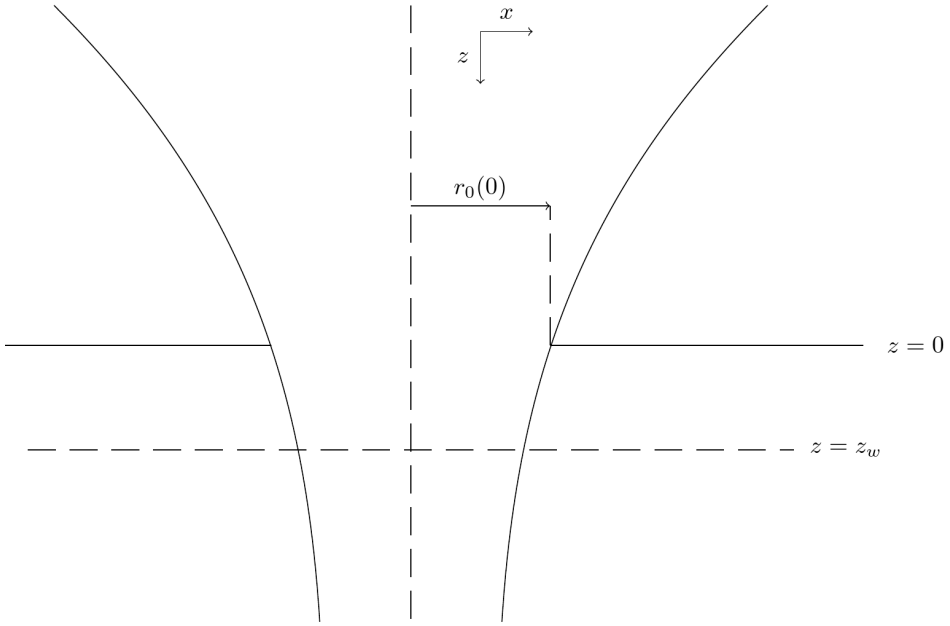

Figure 1: *Scheme of the fluxtube model. The observed radius, $r_0(z)$ and Wilson depression, z_w, are indicated.*

The impact of the influx heat is dependent on the rate at which heat can be transported to the tube by convection in the photosphere and the rate at which this heat can be radiated from the tube. Regarding the heat transported by convection, it is crucial to highlight that close to the tube, the efficiency of radial heat transport by the turbulent flow is reduced. Consequently, near the tube, the heat flux into the tube is primarily carried by radiation. Given that the opacity of the photospheric gas is high (for $z > 0$), this limitation in convective energy transport results in a certain degree of thermal isolation for the tube. This effect will be discussed in Sect. 2.3.

2.2 The diffusion coefficient

It is assumed that radiation and convection are the principal transport mechanisms; especially, energy transport by waves is not considered. We denote the diffusion coefficient as ${}^{in,out}K^{r,c}_{x,z}$ where the index *in* or *out* denotes the inside and outside of the tube, respectively, the index r or c denotes the radiative and convective (or turbulent, as it is called in the original paper from 1976) contributions to K, and x or z denotes the horizontal and vertical components of K. Further, we use the following abbreviations:

$$ {}^{in,out}K^{r} \equiv {}^{in,out}K^{r}_{z} \equiv {}^{in,out}K^{r}_{x} $$

due to radiation diffuses isotropically, i.e. it is the same everywhere, depending only on the local temperature, opacity and density.

$$ {}^{in,out}K_{x,z} \equiv {}^{in,out}K^{r} + {}^{in,out}K^{c}_{x,z}. $$

Far away from the structue, the flux must be vertical and equal to σT^4_{eff}, so that

$$ {}^{out}K_z \partial_z T = \sigma T^4_{eff} \tag{5} $$

This relation is used to calculate ${}^{out}K_z$ from the known temperature distribution in the unperturbed photosphere and convection zone. It is precomputed and smoothed (using the smoothing splines of the 3rd order) to avoid numerical issues due to computing inverse of temperature gradient with height. The data is provided by the solar model described in Sect. 2.5. The key quantities from the model atmosphere are plotted against the geometrical height in Fig. 21 in the Appendix.

It should be noted that energy transport by diffusion is incompatible with a coronal temperature rise; source terms are necessary to describe any distribution ${}^{out}T(z)$ that is not monotonic. This problem is avoided by using a monotonically decreasing temperature and removing corona form the initial model (Sect. 2.5). Additionally, representing the vertical temperature distribution in the convection zone using a diffusion approximation is quite rough, as the flux depends on the difference between the actual and the adiabatic gradient rather than on the gradient itself[3]. This dependence of the flux on the gradient is particularly pronounced in the deeper layers of the convection zone.

The radiative coefficient can be calculated from the Rosseland opacity κ_R:

$$ {}^{out}K^r = \frac{16}{3}\frac{\sigma T^3}{\kappa_R \rho} \tag{6}$$

From Eqs. (5) and (6), follows that

$$ {}^{out}K_z^c = {}^{out}K_z - {}^{out}K^r $$

In order to calculate the horizontal diffusion coefficients, it is essential to recognise that the convective flow is highly turbulent. The convective elements moving laterally have approximately the same mean velocity v (turbulent velocity), and mean free path λ as those moving vertically. It is assumed that since no external force (e.g., gravitation) influences the velocity or energy content of the horizontally moving elements, we can adopt a random walk diffusion coefficient for the transport of heat by these elements. Consequently, the convective component of the horizontal diffusion coefficient is given by the following equation Bond et al., 1966, where c_p is the heat capacity at constant pressure.

$$ {}^{out}K_x^c = \frac{1}{3}\lambda v c_p \rho \tag{7}$$

For v and λ we use the convective velocity and the mixing length from mixing length model of the convection zone, where $\lambda = a_{MLT} H_p(z)$ and H_p is the pressure scale height, $= p/(\rho g)$. To get the total horizontal coefficient we have to add the radiative term from Eq. (6).

The diffusion coefficients adopted for the interior are related to those holding outside by the following relations:

$$ {}^{in}K^r(z) = {}^{out}K^r(z - z_w) \tag{8a}$$

$$ {}^{in}K_z^c(z) = q\, {}^{out}K_z^c(z - z_w) \tag{8b}$$

$$ {}^{in}K_x^c(z) = 0 \tag{8c}$$

Consequently, the radiative coefficient inside the tube is simply shifted downward by the Wilson depression. This is a satisfactory approximation for the observable layers, where energy

[3]The actual gradient is dT/dp computed at every height (using finite differences). The adiabatic gradient is computed for a pair of T and p from equation of state assuming that entropy is constant. This concept comes from mixing length theory, see it in the book of Stix, 2004.

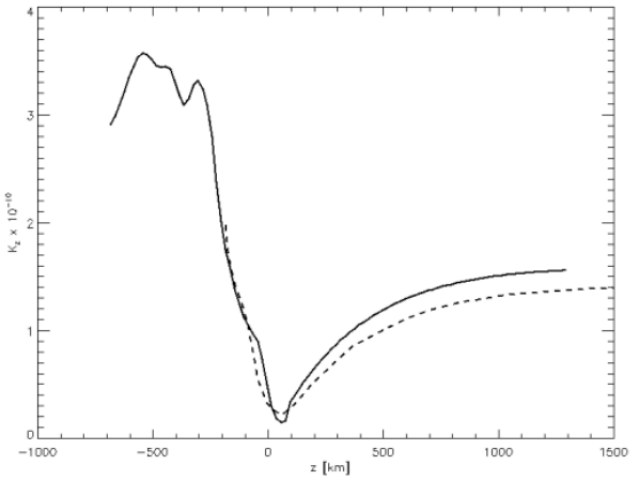

Figure 2: *Smoothed K_z in the model atmosphere (solid) versus the data taken from Fig. 2 Spruit (1976) (dashed). The deviations are expected as the model used to compute K_z is different from the one used in the original paper.*

is primarily transported by radiation. Spruit also shifts the convective coefficient, multiplied by an attenuating factor q, Eq. (8b). This is rough a estimation of ${}^{in}K_z^c(z)$. The value $q = 1$ implies that the magnetic field does not reduce horizontal energy transfer by convection. Given that the temperature at the lower and upper boundaries of the domain are fixed (boundary conditions will be discussed in Sect. 2.4), a reduction of q (for a fixed value of z_w) results in a reduction of the temperature within the tube.

We neglect horizontal convective transport inside the tube, Eq.(8c), because the strong field is supposed to prevent the gas flows across the field that such transport would imply.
We compare K_z with the values from Spruit's Fig. 2 (see Fig. 2) to check if our values are in the same range and have a similar shape to Spruit's. The two curves exhibit a similar shape with a minimum just below the surface. It is worth noting that our curve has a steeper gradient with height. This gradient is computed as a constant over the gradient of the temperature height. Therefore, if our K_z is locally larger than Spruit's, it implies that our temperature gradient is smaller than his (the temperature profile is flatter). The gradient below the surface is determined by the value of the mixing length in the modelling procedure. If necessary, this value can be adjusted to provide a better match. However, the absolute difference between the two curves is relatively small, and it should not significantly affect the solution of our problem.

In his Fig. 2 Spruit shows two more quantities. The *horizontal* Nusselt number N defined as the ratio between the total horizontal diffusivity coefficient and the radiative part of it [4], $N = ({}^{out}K_x^c + {}^{out}K^r)/\,{}^{out}K^r$. The number η gives the same ratio but for the total vertical diffusivity coefficient, $\eta = {}^{out}K_z/\,{}^{out}K^r$. Therefore it, the values in the convection zone are large (10^6 and 10^5, respectively), but they drop ≈ 1 in the photosphere where the radiation dominates.

We can see in Fig. 3 that above the surface, where the radiation dominates, Spruit's curve is nearly constant at 1, while ours rapidly decreases with height. Our result makes no sense because it wolud mean that the $K^r > K_z = K^r + K_z^c$, i.e, that K_z^c is negative.

As previously stated, one of the assumptions made by Spruit is that the diffusion assumption for radiative transfer does not account for the coronal temperature rise. Consequently, he intro-

[4] In the literature, the Nusselt number is usually defined as the ratio between the total heat transfer and the heat transfer by conduction

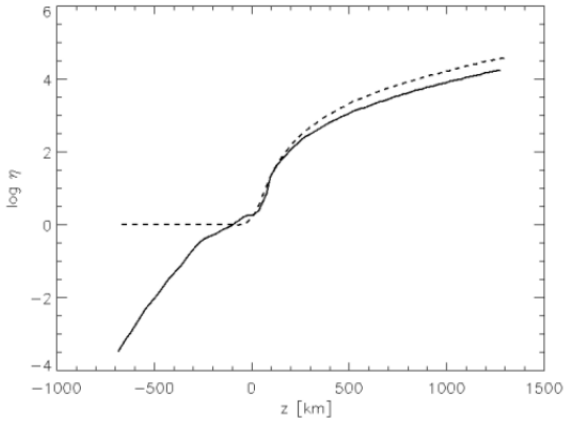

Figure 3: *The ratio between the total vertical diffusivity coefficient K_z and the radiative one computed using the temperature, opacity and density from the model K^r. Our values shown by solid curve, Spruit's are in dashed.*

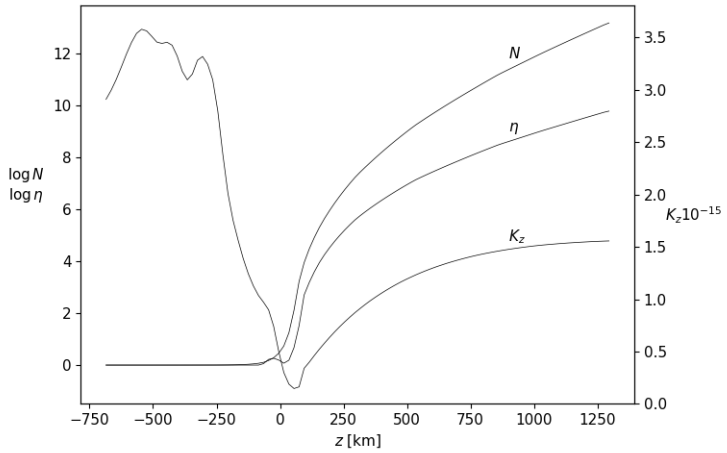

Figure 4: *Diffusion coefficient K_z, the horizontal Nusselt number $N = \left(K_x^c + K^r\right)/K^r$ and the $\eta = K_z/K^r$ in solar convection zone*

duces a monotonically decreasing T above the temperature minimum. However, this statement is somewhat awkward. The diffusion approximation for radiative transfer is only valid deep below the surface, and it fails not only with the temperature rise but already at the photosphere. In the original work it is not specified step-by-step how is this done. From Fig. 3, however, it can be seen that the two curves are broadly similar up to a height of 50 km. Furthermore, Spruit's value of η is found to be equal to unity in this region.

In order to achieve agreement between our η and the original paper, there are two possible approaches. We can correct either K_z or K^r above the height where the two curves of η diverge. Since K_z is determined solely by the effective temperature and the temperature gradient, and K^r is based on an inaccurate assumption, we have chosen to correct K^r. The most straightforward method is to set $K^r = K_z$ above the critical height. This explicit statement of the transfer of energy by radiation above the critical height allows us to conclude that the resulting values depicted in Fig. 4 are accurate. There is a small hump around $z = 0$ in the corrected η, but this should not pose any issues for our flux tube.

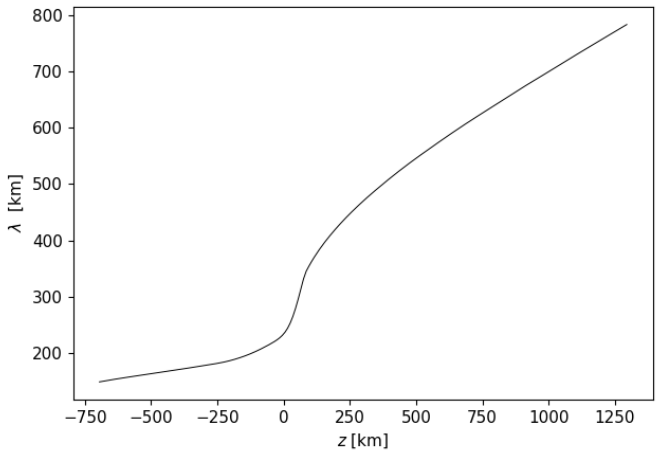

Figure 5: *Mixing length from our model.*

In the following section we will discuss the treatment of the boundary effect near the tube.

2.3 The interface zone between the two components

The model consists of two components: a hotter one representing the unperturbed solar granulation ("out") and a cooler one representing the interior of a flux tube ("in"). These two components are in physical contact at the "wall" between them. However, it is not physically justified or numerically sustainable to assume a hard and sharp wall between two gaseous regimes. Instead, an essential aspect of Spruit's model is the description of this interface zone between the two components. By "description," we mean an estimation of the width and the physical properties of the interface zone between the two components.

A fundamental assumption is that convective elements are unable to penetrate the wall, preventing the transfer of energy across it. Consequently, the efficiency of horizontal convective energy transfer is reduced in the hot component in close proximity to the tube. ${}^{out}K_x^c$ is defined exclusively in terms of Eq. (7):

$$ {}^{out}K_x^c = \frac{1}{3}\lambda(z)v(z)c_P(z)\rho(z) \tag{9}$$

In order to model the reduction in convective energy transfer at the interface, Spruit introduced the concept of attenuated ${}^{out}\tilde{K}_x^c$ and assumed that the attenuation is linearly increasing with distance from the tube, $d = x - x_{wall}$, in the horizontal direction as the wall is approached.

$$ {}^{out}\tilde{K}_x^c(d,z) = \frac{d}{\lambda(z)}\ {}^{out}K_x^c \tag{10}$$

At any height z, it is clear that the attenuation stops at the distance $\lambda(z)$ from the wall:

$$ {}^{out}\tilde{K}_x^c(\lambda(z),z) \equiv {}^{out}K_x^c(z)$$

To know the magnitude of $\lambda(z)$ we compute it from our model, $a_{MLT}H_p$ (initial model detailed in Sect. 2.5), and display it in the figure below. Spruit does not plot λ, but specifies that is around 600 km at $z = 0$ and 1000 km at $z = 200$ km. In our model, λ is smaller for the factor of 2.4 (≈ 250 and ≈ 420 km).

To estimate the effective width of the interface zone, Spruit defines d_c (x_c in his notation) as the distance from the wall outwards where the attenuated convective coefficient ${}^{out}\tilde{K}_x^c$ equates the radiative coefficient ${}^{out}K^r$. From Eq. (10):

$$\frac{d}{\lambda(z)} = \frac{{}^{out}\tilde{K}_x^c}{{}^{out}K_x^c} \Longrightarrow \frac{d_c}{\lambda(z)} = \frac{{}^{out}K^r(d_c,z)}{{}^{out}K_x^c(z)} \Longrightarrow d_c = \frac{{}^{out}K^r(z)}{{}^{out}K_x^c(z)}\lambda(z) \tag{11}$$

The r.h.s can be expressed in terms of the horizontal Nusselt number as

$$d_c = \frac{\lambda(z)}{N(z)-1} \tag{12}$$

Some important remarks: remember that N, by definition, must always be ≥ 1 because the radiative heat transfer cannot be larger than the total one. Above the surface $N \approx 1$, while below the surface it increase rapidly; 100 km below the surface it is already $N \approx 100$ (see the Fig. 4). Formaly, Eq. (12) suggests that $d_c > \lambda$ when $N \in (1,2)$, $d_c < \lambda$ when $N > 2$ and $d_c = \lambda$ when $N = 2$. In the extremum, when $N \longrightarrow 1$, $d_c \longrightarrow \infty$. This is understandable from the physics point of view. In the convectivly stable photosphere, the radiative heat transport prevails and the interface extends to infinity. As N increases with depth much faster than λ, even at small depths below the surface, it holds that $d_c << \lambda$. At these depths, at the distance from the wall $d = d_c$, ${}^{out}\tilde{K}_x^c(d_c,z)$ is not equal to ${}^{out}K_x^c(d_c,z)$, but ${}^{out}\tilde{K}_x^c(d_c,z) = {}^{out}K^r(z)$, meaning that for $d \in (0,d_c)$, i.e. when we get closer to the wall, the radiative heat transfer dominates.

Notice that Spruit approximates

$$d_c(z) = \frac{\lambda(z)}{N(z)-1} \approx \frac{\lambda(z)}{N(z)} \tag{13}$$

This estimation of d_c is only valid in depths where $N(z) >> 1$. Therefore, it is only applicable below the surface. As soon as it becomes meaningful, we observe that d_c is much smaller than the size of the tube or the Wilson depression. Consequently, the purpose of estimating it is not to use its value in the computations, but to emphasise that the interface zone, although theoretically as wide as the mixing length λ, in reality must be sheet-like.

So far we established that the interface zone is more a wall than an extended zone. Let's now estimate what is the temperature jump at the wall at any height z, i.e. what could be the temperature difference at the two sides of the wall. As d_c is very small, we can assume that the horizontal flux close to the wall (i.e. in $d \in (0,d_c)$) is constant with x.

The horizontal flux in the entire zone where ${}^{out}K_x^c(d,z)$ is attenuated, i.e. for $d \in (0,\lambda)$, is given by:

$$F_x(z) = ({}^{out}\tilde{K}_x^c(d,z) + {}^{out}K^r(z))\frac{\partial T(d,z)}{\partial d} = {}^{out}K_x^c(z)\left(\frac{d}{\lambda(z)} + \epsilon(z)\right)\frac{\partial T(d,z)}{\partial d} \tag{14}$$

where

$$\epsilon(z) = \frac{{}^{out}K^r(z)}{{}^{out}K_x^c(z)} = \frac{1}{N(z)-1} \tag{15}$$

From Eq. (14), the temperature gradient in the interface can be written as:

$$\frac{\partial T}{\partial d} = \left(\frac{\lambda}{d+\lambda\epsilon}\right)\frac{F_x}{{}^{out}K_x^c} \tag{16}$$

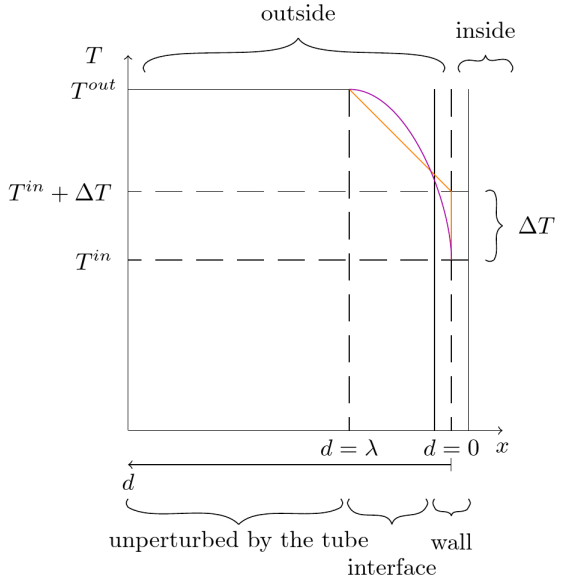

Figure 6: *Scheme of the transition layer.*

which can be formally integrated in the boundaries $(0, d)$ to obtain the temperature at the distance d from the wall:

$$T(d) - T(0) = \frac{\lambda F_x}{{}^{out}K_x^c} \left[\ln\left(\frac{d}{\lambda} + \epsilon\right) - \ln \epsilon \right] \tag{17}$$

A key moment here is to realize that $T(0)$ is the temperature at the cool side of the wall. The horizontal variation of the temperature is set only by the $\ln d$ term as, at a given height, all other terms are independent of d. At the distance $d = \lambda$ the temperature is then

$$T(\lambda) - T(0) = \frac{\lambda F_x}{{}^{out}K_x^c} \left[\ln(1 + \epsilon) - \ln \epsilon \right] \tag{18}$$

Notice that in Eq. (14) we formally write $F_x(d, z)$ as a function of d in contradiction with Eq. (17), where we assumed F_x to be constant. We actually use this assumption explicitly only when we integrate $\partial T/\partial d$ to take F_x out of the integral. When we evaluate the resulting expression at $d = \lambda$, it implies that the $F_x = const$ assumption is made in the entire zone $d \in (0, \lambda)$. However, as we derived $\partial T/\partial z$ from Eq. (14), it has such form that it cancels out the d-dependency of F_x, which is this indeed constant with d with the so defined derivative of T.

From the Fig. 7 we see a typical natural logarithm behaviour: the temperature in this case decrease slowly far from the tube and then very fast close to it. We might get a crazy idea here to approximate this logarithmic temperature variation with a linear variation for $d \in (0, \lambda)$ and with a vertical temperature drop ΔT at $d = 0$. This idea is equivalent to assuming that the convective flux is not attenuated in $d \in (0, \lambda)$ as we will see now[5].

Substituting ${}^{out}\tilde{K}_x^c = {}^{out}K_x^c$ in Eq. (14) gives:

$$F_x(z) = ({}^{out}K_x^c(z) + {}^{out}K^r(z)) \frac{\partial T(d, z)}{\partial d} = {}^{out}K_x^c(z)(1 + \epsilon(z)) \frac{\partial T(d, z)}{\partial d} \tag{19}$$

[5]Actually we can assume it since we demonstrated that $d_c << \lambda$. So, for $d \in (\lambda, d_c)$, ${}^{out}K_x^c \approx {}^{out}\tilde{K}_x^c$. Here the $\approx$ symbol means that ${}^{out}\tilde{K}_x^c$ in that interval is at least as large as K^r.

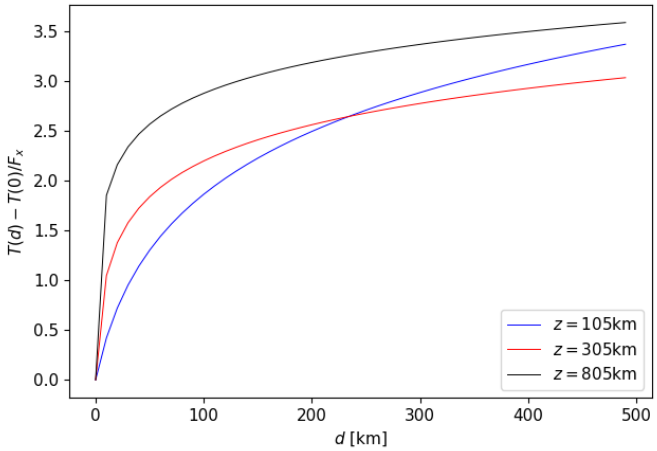

Figure 7: *$T(d,z) - T(0,z)/F_x$ against d for different heights, $T(0) \equiv T(0,z)$.*

and

$$\frac{\partial T}{\partial d} = \left(\frac{1}{1+\epsilon}\right)\frac{F_x}{{}^{out}K_x^c} \tag{20}$$

Again, we integrate in the $(0,d)$ boundaries, but acknowledging that there is an additional vertical drop of ΔT between the points (see Fig. 6):

$$T(d) - T(0) = \Delta T + \int_0^d \left(\frac{1}{1+\epsilon}\right)\frac{F_x}{{}^{out}K_x^c}\mathrm{d}d = \Delta T \frac{F_x}{(1+\epsilon)\,{}^{out}K_x^c}d \tag{21}$$

At $d = \lambda$:

$$T(\lambda) - T(0) = \Delta T \frac{\lambda F_x}{(1+\epsilon)\,{}^{out}K_x^c} \tag{22}$$

Eqs. (18) and (22) give the same temperature drop computed in two different ways (in both derivations we consistently assumed that $F_x = const$), and therefore we can equate the two:

$$\Delta T \frac{\lambda F_x}{(1+\epsilon)\,{}^{out}K_x^c} = \frac{\lambda F_x}{{}^{out}K_x^c}[\ln(1+\epsilon) - \ln\epsilon] \tag{23}$$

$$\Delta T = \frac{\lambda F_x}{(1+\epsilon)\,{}^{out}K_x^c}\left(-\frac{1}{1+\epsilon} + \ln(1+\epsilon) - \ln\epsilon\right) \tag{24}$$

Where ϵ, may now be substituted in terms of the horizontal Nusselt number:

$$\Delta T = \frac{\lambda F_x}{(1+\epsilon)\,{}^{out}K_x^c}\left(\ln N - 1\frac{1}{N}\right) \tag{25}$$

We are not done yet because we don't know the value of F_x. So we replace F_x using Eq. (14):

$$\Delta T = \lambda\left(\frac{d}{\lambda} + \epsilon\right)\left(\ln N - 1\frac{1}{N}\right)\frac{\partial T}{\partial d} = \lambda\left(\frac{d}{\lambda} + \frac{1}{N-1}\right)\left(\ln N - 1\frac{1}{N}\right)\frac{\partial T}{\partial d} \tag{26}$$

Here we certainly know λ and N, but the values of d and the derivative are missing. At this place Spruit is cryptic saying that Eq. (14) is taken at $d = \lambda$ which is easy to apply:

$$\Delta T = \lambda\left(1 + \frac{1}{N-1}\right)\left(\ln N - 1\frac{1}{N}\right)\frac{\partial T}{\partial d} = \lambda\left[\left(\frac{N}{N-1}\ln N\right) - 1\right]\frac{\partial T}{\partial d} \tag{27}$$

and that the derivative is evaluated at the wall ($d = 0$)[6]. While this may imply that the derivative $\partial T/\partial d$ is computed somehow locally at the wall, this is likely misleading interpretation. First, because the numerical part of the motivation to discuss the temperature dependence close to the tube comes from the difficulty to compute the derivative across the discontinuity. Second, because we already placed d with λ in Eq. (14) in the previous step. Remember that we wrote Eq. (14) assuming that the $\partial T/\partial d$ is such that it cancels out the d-dependence of F_x, and thus the definition of the derivative must be related to the choice of d. Therefore, the choice of d suggests that we may interpret $\partial T/\partial d$ as the derivative over the distance λ. On the interval $(0, \lambda)$ the temperature increases from $T^{in} + \Delta T$ to T^{out}. From such interpretation we get:

$$(\partial T/\partial d)_{d\in(0,\lambda)}(z) = \frac{T(d=\lambda, z) - T(d=0, z)}{\lambda(z)} = \frac{T^{out}(z) - (T^{in}(z) + \Delta T(z))}{\lambda(z)} \tag{28}$$

If we use this expression in Eq. (27):

$$\Delta T = \left[\left(\frac{N}{N-1}\ln N\right) - 1\right] T^{out}(z) - (T^{in}(z) + \Delta T(z)) \tag{29}$$

or

$$\Delta T = f(z)(T^{out}(z) - (T^{in}(z) + \Delta T(z))) \tag{30}$$

$$\Delta T = \frac{f(z)}{1+f(z)}(T^{out}(z) - T^{in}(z)) = \phi(z)(T^{out}(z) - T^{in}(z)) \tag{31}$$

The function ϕ is plotted in the Fig. 8a. Above the surface, ϕ is small, and at $z \approx 250$ km ϕ is already ≈ 0.85. In Fig. 8b, ΔT is plotted, note that there is a distinguished peak below the surface. We will see the effect of ΔT in Sects. 5.2 and 5.3.

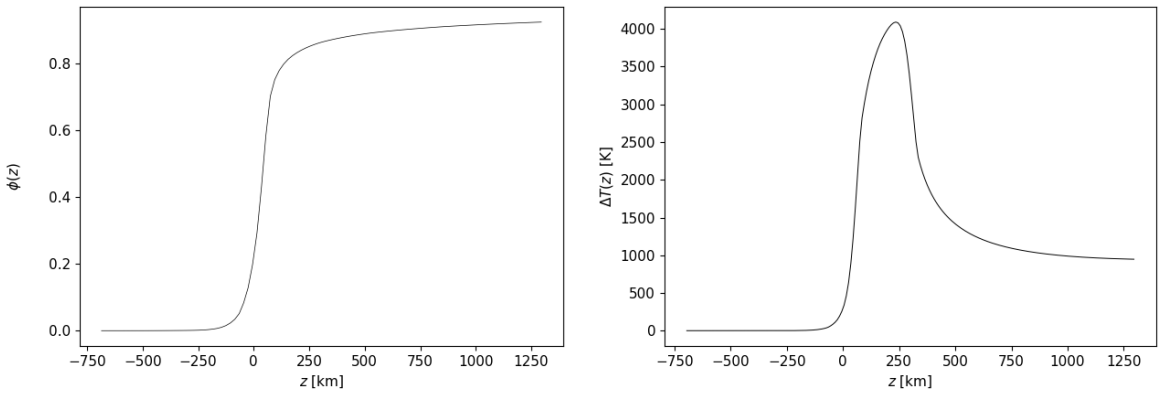

(a) ***(b)***

Figure 8: *Function ϕ at the left panel (a) and $\Delta T(z)$ at the right one (b).*

To avoid numerical issues caused by the steep gradient below the surface, we fixed the temperature at the wall by $\Delta T + T^{in}_{\text{initial}}$.

[6]He changes the labeling of the derivative from ∂x to ∂^{out}_r.

2.4 Boundary conditions

Boundary conditions are crucial in solving partial differential equations as they ensure the uniqueness and stability of the solution. They place the simulation box in contact with the solar interior and atmosphere, and complete the set of equations. Our domain is a vertical cross-section through the Sun and the boundaries include:

- The top boundary representing the interface with the higher atmosphere.
- The bottom boundary, deeper within the convective zone.
- The lateral boundaries, the left one representing horizontal extents and the right one set at the axis of a fluxtube.

Spruit defined the boundary conditions as it follows, taking into account that z-axis is defined positively counted inwards the Sun. At the upper atmosphere we impose the condition that the temperature approaches zero when $z \longrightarrow -\infty$:

$$T = 0 \text{ for } z \longrightarrow -\infty \tag{32}$$

At the bottom of our domain the temperature is fixed by:

$$T = T_0 \text{ for } z = z_0 \tag{33}$$

As $x \longrightarrow \infty$ the temperature T approaches the solution (T_1) of the differential equation $K_z \partial_{zz} T + dK_z/dz \cdot \partial_z T = 0$ with Eqs. (32) and (33) as boundary conditions, and K_x and K_z are the coefficients for horizontal and vertical transport, respectively. We impose:

$$T = T_1 \text{ for } x \longrightarrow \infty \tag{34}$$

At the axis of the fluxtube, we impose a symmetry condition by:

$$\partial T/\partial x = 0 \text{ for } x = 0 \tag{35}$$

As we will see in Sect. 3, we also have to define boundary conditions for the diffusion coefficients. For the left and right boundaries, we assume no variation in K_x along the horizontal direction:

$$\partial K_x/\partial x = 0 \text{ for } x = 0 \text{ and } x \longrightarrow \infty \tag{36}$$

For the top and bottom boundaries, we also assume no variation in K_z along the vertical direction:

$$\partial K_z/\partial z = 0 \text{ for } z = z_0 \text{ and } z \longrightarrow -\infty \tag{37}$$

2.5 Initial model atmosphere

Spruit, 1976, specifies that his initial model for the unperturbed atmosphere is a combination of the HSRA model (Gingerich et al., 1971) in the atmospheric part, the VAL model (Vernazza et al., 1973) around $\tau = 1$, and the mixing-length 1D model of the solar convection zone from his earlier paper (Spruit, 1974). The exact way how these models were combined is not detailed. In this thesis, I rely on the method described in great detail by Perdomo García (2023). She adopts the HSRA model for the atmosphere and then integrates the temperature and pressure inwards to satisfy the solar flux and the condition of the hydrostatic equilibrium (HSE). The free parameter of the model is the mixing length (a_{MLT}) which is taken to be 1.6 in the units of the

pressure-scale height. Once the model is converged, the density is evaluated using precomputed tables of the equation of state assuming the realistic solar abundances (Asplund et al., 2009) and the Rosseland opacity is computed using the data from the ATLAS9 code (Kurucz, 2014). The geometrical height scale is obtained by the reversed integration of HSE. Finally, the model is interpolated to a uniform geometrical height scale with $\mathrm{d}z = 5\,\mathrm{km}$.

In all numerical experiments presented in this thesis, the initial models in the photosphere extends 2 Mm in the vertical direction. Roughly 1/3 is above $\tau = 1$.

2.6 Pressure

So far we were busy with the heat diffusion equation only (i.e. the energy equation (1c) in the form of Eq. (2b)). To compute the pressure (p) and the density (ρ), we have to close the system by adding the hydrostatic equation (2a) and the equation of state for which we will assume the ideal gas equation. For the given temperature distribution, the pressure is computed column by column in the following way.

We start from the ideal gas law:

$$p = \rho \mathcal{R} T / \mu \tag{38}$$

where ρ can be written as $\rho = p\mu/(\mathcal{R}T)$. On the other hand, we consider the equation of hydrostatic equilibrium:

$$\frac{dp}{dz} = -\rho g \tag{39}$$

combining these two equations we have:

$$\frac{dp}{p} = \frac{-\mu g}{\mathcal{R}T} dz \tag{40}$$

By integrating Eq. (40) at the axis of the tube starting from the upper atmosphere, we obtain:

$$\log p = -\frac{\mu g}{\mathcal{R}T} z + \mathrm{C} \tag{41}$$

The coordinate system defined in this model have the vertical direction in the same direction as gravity, so we have to change the sign of the Eq. (41), and thus we get:

$$\log p(x,z) = \frac{\mu g}{\mathcal{R}T(x,z)} z + \mathrm{C} \Longrightarrow p(x,z) = p_0 \exp\left(\frac{\mu g z}{\mathcal{R}T}\right) \tag{42}$$

where p_0 is the pressure at the upper boundary.
As we see the solution depends critically on the integration constant p_0 which has meaning of the pressure at the top of the computational box and it may vary from one vertical column to another. Spruit imposes that the magnetic field at the axis of the tube is vertical, so it does not create vertical force in that column and the gas determined in the procedure described above is the internal gas pressure. Moreover, the 1976 paper says that "the integration constant is fixed iteratively by demanding that $\tau_{5000}(z_w) = 1$ " without specifying the details of the iterative procedure[7].

The algorithm that we used consists in the following steps:

[7]Spruit uses τ_{5000} but we will use τ to simplify the nomenclature.

1. We initially assume that p_0 is equal to the value of the pressure at the top of the initial atmosphere that we can read from the model described in the previous section.

2. For the 1D temperature stratification along the axis we integrate the pressure equation (42). We approximate that the mean molecular weight $\mu = 1.26$ is constant with height. Other constants are the universal gas constant $\mathcal{R} = 8.3145 \cdot 10^7$ erg·K^{-1}·mol^{-1} and the gravity acceleration at the solar surface $\log_{10} g \approx 4.44$ cm/s^2.

3. Using the same temperature stratification and the pressure computed in the previous step, for every height, we interpolate a precomputed table of the opacity at 5000 $\mathring{A}$ as a function of T and p. The result is the opacity κ.

4. Using the ideal gas law, Eq. (38), from T and p we compute the density ρ at every height.

5. Using ρ and κ, we integrate the optical depth as:

$$\tau(z) = \int_0^z \kappa \, \rho \, dz$$

   taking that the optical depth at the top of the atmosphere is equal to 0. The optical depth is building up quickly with depth, so this assumption has very little impact and only close to the top boundary.

6. We interpolate the τ scale to find the geometrical height at which $\tau = 1$, z_0

7. The height z_0 is compared with the height that corresponds to the z_w value of that model, $z(z_w)$. If the computed z_0 is higher than $z(z_w)$, it means that the opacity is too small, hence that the pressure is too low and, therefore, that the initially assumed p_0 has to be increased.

8. We keep repeating these steps until the convergence. For the convergence criterion we use relative error of 10^{-2} in τ at $z(z_w)$.

To test the steps of the described procedure, we first apply it to the initial atmospheres T^{in} and T^{out}. Fig. 9 show the data from the two initial models (thick curves) and the quantities computed using our procedure (thin curves). The match is very good in both pairs of models (solid curves: model outside; dashed curves: model inside of the tube) except below the surface where our assumption on $\mu = \text{const}$ fails due to extensive hydrogen ionization. The blue and red solid curve show the quantities computed from the temperature stratification along the axis of the Model E (see Table 2, we will present all the models in Sect. 5.2). The red curve is obtained taking p_0 to be equal to the pressure at the top of the initial model outside of the tube; the blue curve, p_0 is equal to the pressure at the top of the initial model inside of the tube. In the figure showing the optical depth, we over-plotted vertical (dash-triple-dotted) lines to indicate heights where $\tau = 1$ for the tube-axis model when the initial guess p_0 is set to the two extreme values. The green vertical line indicates the height 200 km below the $\tau = 1$ in the initial model outside. Our iterative fix has to find the value of p_0 such that $\tau = 1$ of the axis model falls at the height indicated by the orange vertical line in that plot.
The magenta curve in the same figure shows the converged solution. In this particular case it is obtained with $p_0 = 40.8$ dyn·cm^{-2} (p_0 corresponding to the blue and red curve is correspondingly 23.2 and 229.4 dyn·cm^{-2}.

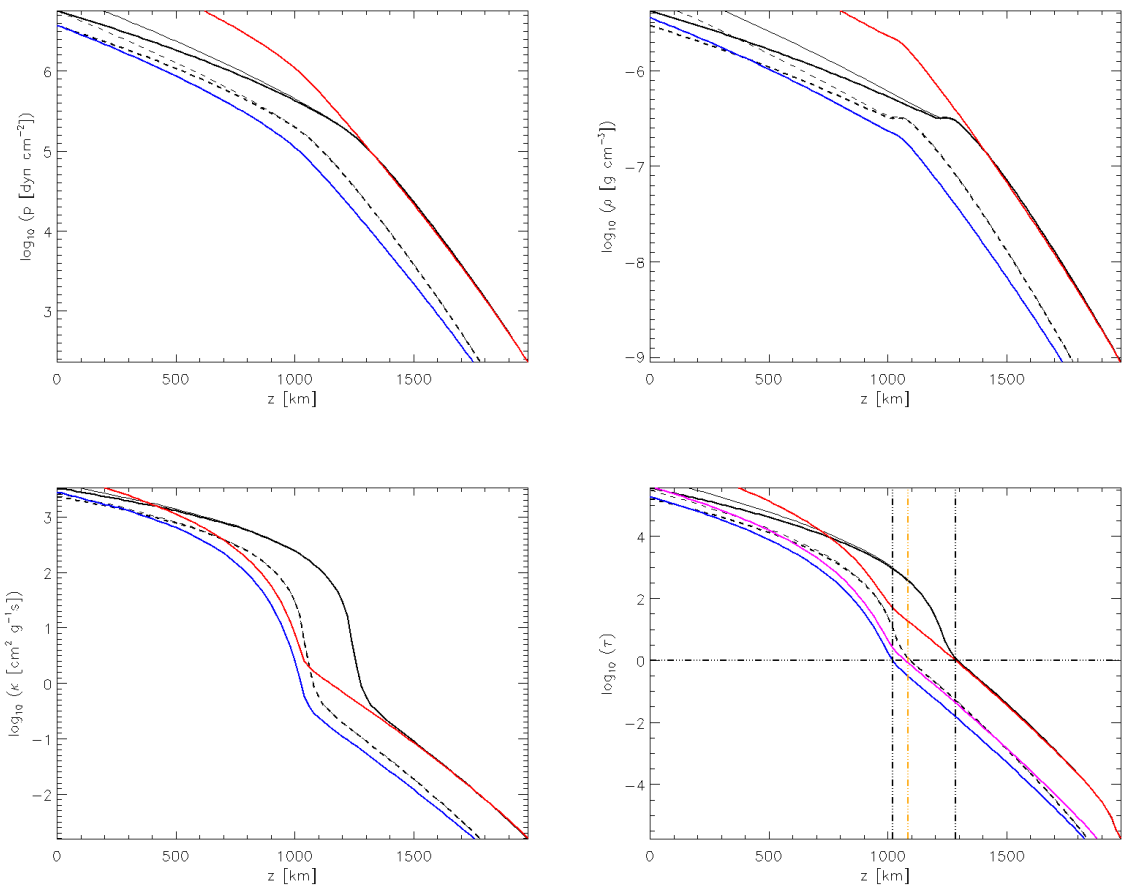

Figure 9: *From left to right and top to bottom: pressure, density, opacity and optical depth. Thick curves represents the values from the initial model, and thin curves represents the results of our procedure (solid line: outside the tube, dashed line: inside the tube). The blue and red solid line shows the quantities computed of the model E (see Table 2). The red one shows the result of the procedure taking p_0 at the top of the initial model outside the tube and the blue one p_0 is the value at the top inside the tube.*

However, with this procedure p_0 is fixed only along the axis and in the quiet-Sun column furthest from the tube where we assume (by setting the boundary condition) that the final solution is fixed by the initial model atmosphere. In all other points in between, in principle, we do not know what is the expected local Wilson depression. Assuming that the Wilson depression is constant throughout the tube is equivalent to assuming that the temperature is homogeneous in the tube which is obviously not the case in any of our models. In Fig. 10, we show the radial variation of p_0 in three cases:

1. The algorithm is blindly applied taking that z_w is constant throughout the tube.

2. The algorithm is applied at the axis ($z_w = 200$ km), and at the quiet-Sun boundary and all the columns outside the tube ($z_w = 0$ km). Within the tube, p_0 is not computed, but gradually and smoothly scaled with a cosine function between the two values of p_0, the one at the top outside the tube and the shifted value.

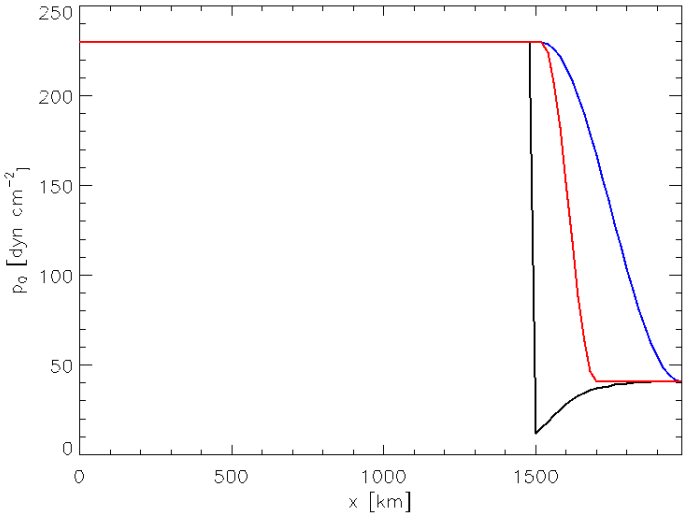

Figure 10: *Radial variation for the initial pressure in the three cases mentioned (1, 2, and 3 in black, blue and red respectively).*

3. Outside the tube p_0 is computed identical as the variant 2, but in the tube scaled only in the first 200 km from the wall inwards. Elsewhere computed using the algorithm with $z_w = 200$ km.

The radial change of p_0 for the three variants is shown in Fig. 10: variants 1, 2, and 3 in black, blue and red respectively. Fig. 10 shows the integration constant for pressure at the top of the domain. The integration constant for each column is a free parameter of the problem. By setting it non-constant with x, we roughly mimic the pressure drop due to the magnetic field (the temperature drop we've mimicked by shifting the inner model by z_w). The results of the application of the three variants will be discussed in Sect. 5.3.

3 Numerical solution of the diffusion equation

In general terms, the diffusion equation with constant diffusion coefficient is written as

$$\frac{\partial u}{\partial t} = K\Delta u + S \tag{43}$$

where u is the quantity being diffused, K is the constant diffusion coefficient, S is the source term, and Δ is Laplacian. If the quantity is the temperature, this equation is called *heat equation*. Our aim is to calculate all energy transport (both radiation and convection) using a steady state diffusion approximation (SDE). Thus the temperature distribution satisfies:

$$\nabla \cdot (K\nabla T) = 0 \tag{44}$$

To achieve this goal, in this section we will build a numerical scheme step-by-step from the more simplistic one-dimensional situation to the two-dimensional regime with variable and anisotropic diffusion coefficient.

3.1 One dimension, steady state with constant diffusion coefficient

We start with the simplest case: the one-dimensional Laplace equation

$$\frac{\partial^2 u}{\partial z^2} = 0 \tag{45}$$

To solve it numerically, we discretised the z-axis on a grid $\{z_i\}_{i=0}^{n-1}$ with $z_{i+1} - z_i = h = const$. At each inner point ($i \in [1, n-2]$) the derivative is computed using the second order finite central difference (FCD) formula:

$$\left(\frac{\partial^2 u}{\partial z^2}\right)_i = \frac{u_{i+1} - 2u_i + u_{i-1}}{h^2} \tag{46}$$

So for each inner point the equation becomes a linear algebraic equation:

$$\frac{u_{i+1} - 2u_i + u_{i-1}}{h^2} = 0 \tag{47}$$

At the end points, this equation does not apply. Consequently, one has to describe boundary conditions (BC). There are two main strategies for describing BC. Dirichlet's condition consists of specifying the values of the function u at the boundary, Neumann's condition consists of specifying the values of its derivative $\partial u/\partial z$ at the boundary. We will use Dirichlet's condition.

In Laplace equation, the BC is the key that fully specifies the behaviour and the type of solution.

To use this equation in all the grid points, we consider two additional grid points (z_{-1} and z_n), called *ghost points* or *ghost zone*, and their corresponding values (u_{-1} and u_n), where we will set the BC. With this scheme we are able to use Eq. (47) at all grid points and it represents a system of n linear equations for n unknowns (u_i).

We can now write the system in the matrix form:

$$\mathbf{A}u = -s \tag{48}$$

where, form $n = 4$ and including BC, and ghost points:

$$\mathbf{A} = \begin{pmatrix} 1 & 0 & 0 & 0 & 0 & 0 \\ D & C & U & 0 & 0 & 0 \\ 0 & D & C & U & 0 & 0 \\ 0 & 0 & D & C & U & 0 \\ 0 & 0 & 0 & D & C & U \\ 0 & 0 & 0 & 0 & 0 & 1 \end{pmatrix}, \; u = \begin{pmatrix} u_{-1} \\ u_0 \\ u_1 \\ u_2 \\ u_3 \\ u_4 \end{pmatrix}, \; s = \begin{pmatrix} -u_{-1} \\ 0 \\ 0 \\ 0 \\ 0 \\ -u_4 \end{pmatrix} \tag{49}$$

where U, C and D stand for the upwind, central and downwind coefficients:

$$U = \frac{1}{h^2}, C = -\frac{2}{h^2}, D = \frac{1}{h^2} \tag{50}$$

Note that the source vector is only different from zero in the first and last row to represent the BC. One can also write the system by including the BC in the first and last equations (for the grid points only), where the boundary conditions now become source terms in the first and last row:

$$\mathbf{A} = \begin{pmatrix} C & U & 0 & 0 \\ D & C & U & 0 \\ 0 & D & C & U \\ 0 & 0 & D & C \end{pmatrix}, \; u = \begin{pmatrix} u_0 \\ u_1 \\ u_2 \\ u_3 \end{pmatrix}, \; s = \begin{pmatrix} -\frac{u_{-1}}{h^2} \\ 0 \\ 0 \\ 0 \\ -\frac{u_4}{h^2} \end{pmatrix} \tag{51}$$

This system is clearly a three-diagonal system of linear equations which can be solved by the direct method of Gaussian elimination, but also by an indirect, iterative method. There are three commonly used methods known as Jacobi, Gauss-Seidel (GS) and successive overrelaxation (SOR) (Varga, 2000). The implementation of the three methods is very similar.

3.2 One dimension, steady state with variable diffusion coefficient

Our next step is to solve the 1D equation at steady state with a variable diffusion coefficient. To solve this equation, we start from Fick's first law, which states that the diffusion flux F is proportional to the concentration gradient.

$$F = -K\frac{\partial u}{\partial z} \tag{52}$$

The diffusion equation (Fick's second law) is derived from the previous equation and from the mass conservation equation

$$\frac{\partial u}{\partial t} = \nabla(K\nabla u) \tag{53}$$

where K can be variable. In one-dimension and for the steady state allowing the sources s, it is written as it follows:

$$\frac{\partial}{\partial z}\left(K(z)\frac{\partial u}{\partial z}\right) = -s \tag{54}$$

To discretize this expression we consider the stencil $(i-1, i, i+1)$. We begin finding the two first derivatives in the first order of accuracy at $(i-1, i)$ and $(i, i+1)$.

$$u'_{i-\frac{1}{2}} = \frac{u_i - u_{i-1}}{h}, \; u'_{i+\frac{1}{2}} = \frac{u_{i+1} - u_i}{h} \tag{55}$$

These derivatives are not equal at point i as, in the first order of accuracy, the function u is piece-wise linear. Therefore, the two derivatives have the meaning of the left and the right derivative at the point i. The second derivative of u at the point i is the first derivative, again in the first order of accuracy of Eq. (55) :

$$u''_i = \frac{u_{i+\frac{1}{2}} - u_{i-\frac{1}{2}}}{h} = \frac{u_{i+1} - 2u_i + u_{i-1}}{h^2} \tag{56}$$

This expression is identical to the expression for the second derivative in the second order of accuracy by the method of FCD, this is important to remember when higher-order finite central differences are implemented.

Now we consider the derivative in Eq. (54), as K is not constant we have to consider some approximation for K to discretize the derivative. There are two easy choices:

(a) 0th order approximation: it is assumed that K is constant within the interval $(i-\frac{1}{2}, i+\frac{1}{2})$, $K = const = K_i$. In that case:

$$\frac{\partial}{\partial z}\left(K(z)\frac{\partial u}{\partial z}\right)_i = \frac{K_i(u'_{i+\frac{1}{2}} - u'_{i-\frac{1}{2}})}{u} = \frac{K_i(u_{i+1} - 2u_i + u_{i-1})}{h^2} \tag{57}$$

However, notice that the intervals on which K and u' are approximated do not match. K is set on $(i-\frac{1}{2}, i+\frac{1}{2})$ and u'' on $(i-1, i)$.

(b) 1st order approximation (piece-wise linear): it is assumed that K is a linear function between the centers of the grid cells, i.e. at the interval $(i-1, i)$,

$$K = \frac{K_i - K_{i-1}}{z_i - z_{i-1}}(z - z_{i-1}) + K_{i-1} \tag{58}$$

so, for the intermediate points:

$$K_{i-\frac{1}{2}} = \frac{K_i - K_{i-1}}{h}\frac{h}{2} + K_{i-1} = \frac{K_i + K_{i-1}}{2},\ K_{i+\frac{1}{2}} = \frac{K_{i+1} + K_i}{2} \tag{59}$$

The entire term now becomes:

$$\frac{\partial}{\partial z}\left(K(z)\frac{\partial u}{\partial z}\right)_i = \frac{K_{i+\frac{1}{2}}u'_{i+\frac{1}{2}} - K_{i-\frac{1}{2}}u'_{i-\frac{1}{2}}}{h} = \frac{(K_{i+1} + K_i)(u_{i+1} - u_i) - (K_i + K_{i-1})(u_i - u_{i-1})}{2h^2} \tag{60}$$

Notice that this method requires a 3-points stencil $(i-1, i, 1+1)$.

In what follows, the option (b) will be used.

The diffusion equation for the inner points is then:

$$\frac{(K_{i+1} + K_i)u_{i+1} - (K_{i+1} + 2K_i + K_{i-1})u_i + (K_i + K_{i-1})u_{i-1}}{2h^2} = -s_i \tag{61}$$

In the matrix form, and for $n = 4$, this equation is written as follows:

$$\mathbf{A}u = -s \tag{62}$$

$$\mathbf{A} = \begin{pmatrix} C_0 & U_0 & 0 & 0 \\ D_1 & C_1 & U_1 & 0 \\ 0 & D_2 & C_2 & U_2 \\ 0 & 0 & D_3 & C_3 \end{pmatrix},\ u = \begin{pmatrix} u_0 \\ u_1 \\ u_2 \\ u_3 \end{pmatrix},\ s = \begin{pmatrix} \frac{(K_0+K_{-1})u_{-1}}{2h^2} \\ 0 \\ 0 \\ \frac{(K_3+K_4)u_4}{2h^2} \end{pmatrix} \tag{63}$$

where U_i, C_i and D_i stand for:

$$U_i = \frac{K_i + K_{i-1}}{2h^2},\ C_i = -\frac{K_{i+1} + 2K_i + K_{i-1}}{2h^2} \equiv U_i + D_i,\ D_i = \frac{K_{i+1} + K_i}{2h^2} \tag{64}$$

It is important to notice that in this case boundary conditions must be specified both for K and u.

3.3 Two dimensions, steady state with constant diffusion coefficient

The next step is to solve the diffusion equation in two dimensions, with constant diffusion and steady state. In Cartesian coordinates this equation is written as:

$$K\Delta u(x,z) = K\left(\frac{\partial^2 u(x,z)}{\partial x^2} + \frac{\partial^2 u(x,z)}{\partial z^2}\right) = 0 \tag{65}$$

The two derivatives of second order are discretized as before but now taking care that $u(x,z) = u_{i,j}$, so the derivatives are written as follows:

$$\left(\frac{\partial^2 u}{\partial x^2}\right)_{i,j} = \frac{u_{i+1,j} - 2u_{i,j} + u_{i-1,j}}{h_x^2} \tag{66}$$

$$\left(\frac{\partial^2 u}{\partial z^2}\right)_{i,j} = \frac{u_{i,j+1} - 2u_{i,j} + u_{i,j-1}}{h_z^2} \tag{67}$$

Therefore in the (i,j) point, the equation becomes

$$K\left(\frac{1}{h_x^2}u_{i+1,j} + \frac{1}{h_x^2}u_{i-1,j} + \frac{1}{h_z^2}u_{i,j+1} + \frac{1}{h_z^2}u_{i,j-1} - 2\left(\frac{1}{h_x^2} + \frac{1}{h_z^2}\right)u_{i,j}\right) = 0 \tag{68}$$

If the horizontal and vertical grid spacing are equal, $h_x \equiv h_z \equiv h$, the previous equation simplifies as

$$K\left(\frac{1}{h^2}u_{i+1,j} + \frac{1}{h2}u_{i-1,j} + \frac{1}{h^2}u_{i,j+1} + \frac{1}{h^2}u_{i,j-1} - \frac{4}{h^2}u_{i,j}\right) = 0 \tag{69}$$

The coefficients will now be called as U (up $= i, j-1$), D (down $= i, j+1$), L (left $= i-1, j$), R (right $= i+1, j$) and C (central $= i, j$). Therefore, the equation for the point i, j reads

$$R_{i,j}u_{i+1,j} + L_{i,j}u_{i-1,j} + D_{i,j}u_{i,j+1} + U_{i,j}u_{i,j-1} - C_{i,j}u_{i,j} = 0 \tag{70}$$

Again, the system can be written in the matrix form $\mathbf{A}u = 0$. But the $n_x \times n_z$ linear equations cannot be sorted uniquely as in the $1D$ case. It is of critical interest at this point to establish a clear nomenclature.

When the elements of matrix $\mathbf{A}$ are written explicitly, one has to choose *column-major* or *row-major* order. We opt for the *row-major* order, meaning that we first increase the horizontal index i and then j. Therefore, the equations for $n_x = n_z = 6$ are ordered as:

$$\begin{gathered}
R_{0,0}u_{1,0} + L_{0,0}u_{-1,0} + U_{0,0}u_{0,-1} + D_{0,0}u_{0,1} - C_{0,0}u_{0,0} = 0, \\
R_{1,0}u_{2,0} + L_{1,0}u_{0,0} + U_{1,0}u_{1,-1} + D_{1,0}u_{1,1} - C_{1,0}u_{1,0} = 0, \\
\cdots = 0, \\
R_{5,0}u_{6,0} + L_{5,0}u_{4,0} + U_{5,0}u_{5,-1} + D_{5,0}u_{5,1} - C_{5,0}u_{5,0} = 0, \\
R_{0,1}u_{1,1} + L_{0,1}u_{-1,1} + U_{0,1}u_{0,0} + D_{0,1}u_{0,2} - C_{0,1}u_{0,1} = 0, \\
\cdots = 0, \\
\cdots = 0, \\
R_{5,5}u_{6,5} + L_{5,5}u_{4,5} + U_{5,5}u_{5,4} + D_{5,5}u_{5,6} - C_{5,5}u_{5,5} = 0
\end{gathered} \tag{71}$$

Once these equations are placed into the matrix $\mathbf{A}$, it is clear that the system is not anymore three-diagonal one. In the lack of sources in Laplace's equation, the source term contains the boundaries, but now they are not only in the first and the last term as in the one-dimension case.

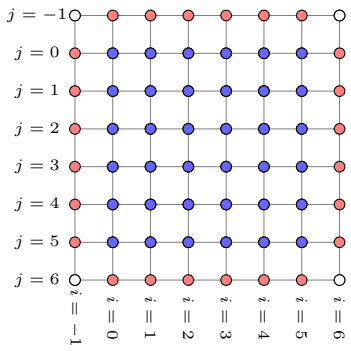

Figure 11: *An example of a 2D grid of* 6×6 *grid points. The solution of the system is evaluated in the blue points. These points are called* ***inner points****. For every blue point there is one linear equation. The boundary condition must be specified in all red points. These are* ***ghost*** *or* ***boundary*** *points. The white points in the corners are not used in the scheme considered here. In a different numerical scheme they may play a role.*

Each of the $n_x \times n_z$ Eq. (71) can be solved in terms of the central point $u_{i,j}$:

$$u_{i,j} = \frac{1}{C_{i,j}}(R_{i,j}u_{i+1,j} + L_{i,j}u_{i-1,j} + U_{i,j}u_{i,j-1} + D_{i,j}u_{i,j+1}) \tag{72}$$

Using Jacobi method to solve this system can be summarized as:

1. Set an initial guess of $u_{i,j}$ in all inner grid points
2. Apply the boundary condition in all ghost points
3. Compute the new quantity $u_{i,j}^{\text{new}}$ as

$$u_{i,j}^{\text{new}} = \frac{1}{C_{i,j}}(R_{i,j}u_{i+1,j} + L_{i,j}u_{i-1,j} + U_{i,j}u_{i,j-1} + D_{i,j}u_{i,j+1}) \tag{73}$$

   This expression can be evaluated in all inner points, including those in the edges, once the boundary condition is set.

4. Evaluate the relative difference between the old and the new values of $u_{i,j}^{\text{new}}$ in all inner points:

$$\varepsilon_{i,j} = \frac{\left|u_{i,j}^{\text{new}} - u_{i,j}\right|}{u_{i,j}}$$

5. If $\varepsilon_{i,j}$ is larger in any point than a specified tolerance ξ, define $u_{i,j} = u_{i,j}^{\text{new}}$ and repeat from step 2, until $\varepsilon_{i,j} < \xi$ in all points.

When the procedure is completed, in every inner point of the grid the last computed $u_{i,j}$ is an approximation to the correct solution with a relative error smaller than the tolerance.

To solve this system with the Gauss-Seidel method, the only difference with the Jacobi method is that, when $u_{i,j}^{\text{new}}$ is computed in one point, the new value is immediatelly stored in $u_{i,j}$. The old solution has to be saved for checking the exit criterion. This method is faster than Jacobi method as it uses updated values as they are computed.

Futhermore, to use the SOR method, the Eq. (73) is now adapted as:

$$u_{i,j} = (1-\omega)u_{i,j} + \frac{\omega}{C_{i,j}}(R_{i,j}u_{i+1,j} + L_{i,j}u_{i-1,j} + U_{i,j}u_{i,j-1} + D_{i,j}u_{i,j+1}) \tag{74}$$

where ω is a constant parameter. Usually taking $\omega \in [1.2, 1.4]$ gives a significant speed-up in respect to Gauss-Seidel and does not compromise stability of the method. If $\omega = 1$, the Gauss-Seidel method is recovered.

3.4 Two dimensions, steady state with variable diffusion coefficient

Finally we will solve the two-dimensions equation, assuming steady state with variable diffusion coefficient.

There are two distinctive case depending on the behavior of K. When the diffusion is isotropic, K is a scalar defined in every point of the grid, $K = K(x, z)$, when it is anisotropic. In the later case, in three-dimensions, $\mathbf{K}$ is s symmetric 3×3 tensor:

$$\mathbf{K} = \begin{pmatrix} K_{x,x} & K_{x,y} & K_{x,z} \\ K_{x,y} & K_{y,y} & K_{y,z} \\ K_{x,z} & K_{z,y} & K_{z,z} \end{pmatrix}$$

while in 2D it reduces to a 2×2 tensor

$$\mathbf{K} = \begin{pmatrix} K_{x,x} & K_{x,z} \\ K_{x,z} & K_{z,z} \end{pmatrix}$$

Further, we assume that the diffusion coefficient has only horizontal and vertical components (cross-components are zero), because the transport processes to be modelled are anisotropic and occur mainly along these two directions. This assumption is particularly relevant in our context, where physical conditions constrain the movement of heat and particles.

$$\mathbf{K} = \begin{pmatrix} K_{x,x} & 0 \\ 0 & K_{z,z} \end{pmatrix}$$

In this situation, the steady diffusion equation in the Cartesian coordinates becomes:

$$\nabla \cdot (\mathbf{K}\nabla u) = \frac{\partial}{\partial x}\left(K_x \frac{\partial u}{\partial x}\right) + \frac{\partial}{\partial z}\left(K_z \frac{\partial u}{\partial z}\right) = 0 \tag{75}$$

To discretize Eq. (75), we can use Eq. (60) as a guide:

$$\begin{aligned} \left(\tfrac{\partial}{\partial x}\left(K_x \tfrac{\partial u}{\partial x}\right)\right)_{i,j} &= \tfrac{1}{2h^2}\left((K_{x;i+1,j} + K_{x;i,j})(u_{i+1,j} - u_{i,j}) - (K_{x;i,j} + K_{x;i-1,j})(u_{i,j} - u_{i-1,j})\right) \\ \left(\tfrac{\partial}{\partial z}\left(K_z \tfrac{\partial u}{\partial z}\right)\right)_{i,j} &= \tfrac{1}{2h^2}\left((K_{z;i,j+1} + K_{z;i,j})(u_{i,j+1} - u_{i,j}) - (K_{z;i,j} + K_{z;i,j-1})(u_{i,j} - u_{i,j-1})\right) \end{aligned} \tag{76}$$

In any inner point (i, j), Eq. (72) remains identical as before, but the coefficients are now

differently defined:

$$\begin{aligned} R_{i,j} &= \tfrac{1}{2h^2}(K_{x;i+1,j} + K_{x;i,j}) \\ L_{i,j} &= \tfrac{1}{2h^2}(K_{x;i,j} + K_{x;i-1,j}) \\ U_{i,j} &= \tfrac{1}{2h^2}(K_{z;i,j} + K_{z;i,j-1}) \\ D_{i,j} &= \tfrac{1}{2h^2}(K_{z;i,j+1} + K_{z;i,j}) \end{aligned} \tag{77}$$

$$C_{i,j} = -\tfrac{1}{2h^2}(K_{x;i+1,j} + 2K_{x;i,j} + K_{x;i-1,j} + K_{z;i,j+1} + 2K_{z;i,j} + K_{z;i,j-1})$$

The numerical solution, remains the same as before. However, now the boundary condition for both K_x and K_z has to be specified.

4 Radiative transfer

To explore how does the intensity contrast between magnetic element and unperturbed photosphere depends on the model parameters, it is necessary to solve radiative transfer equation (RTE) in local thermodynamical equilibrium (LTE) in plane-parallel atmosphere:

$$\frac{\mathrm{d}I}{\mathrm{d}s} = \kappa\rho(B - I) \tag{78}$$

where I is the specific intensity, κ is the absorption coefficient per gram (i.e. the opacity), ρ is the mass density, B is the source function which in LTE is approximated by Planck's function and s is the geometrical scale along the ray. If the RTE is written for one specific wavelength (for example, 5000 Å), then it is called "monochromatic" and index ν is added to wavelength dependent quantities I_ν, B_ν and κ_ν. Commonly the RTE is written in terms of the optical depth scale τ:

$$\tau = \kappa\rho\mathrm{d}s \tag{79}$$

Along the same ray optical depth differ depending on the direction in which it is evaluated. As it is commonly computed from the top downward and instead of s is used the height in the atmosphere (increasing from the bottom upward), sometimes a minus sign appears in Eq. 79. The RTE in this form, when the source function is known, can be integrated formally along a short segment of the ray (so called a "short characteristic"), between two successive grid points $i-1$ and i:

$$I_i = I_{i-1}\,\mathrm{e}^{-(\tau_i - \tau_{i-1})} + \int_{\tau_{i-1}}^{\tau_i} B(t)\mathrm{e}^{-(\tau_i - t)}\,\mathrm{d}t \tag{80}$$

This solution is known as the "formal solution" of the RTE. The first term represents the intensity in the previous point along the ray I_{i-1} diminished for the absorption along the ray $\mathrm{e}^{-(\tau_i-\tau_{i-1})}$. The second term represents the contribution of Planck's emission to the intensity along the characteristic. To evaluate the intensity in the point i therefore one needs to evaluate the difference in the optical depths $\Delta\tau = \tau_i - \tau_{i-1}$ and the radiative integral in Eq. 80. There are numerous methods that can be implemented for this task. We opted for the simplest one, the method of short-characteristics (Olson et al., 1987) in the first order of accuracy, which means

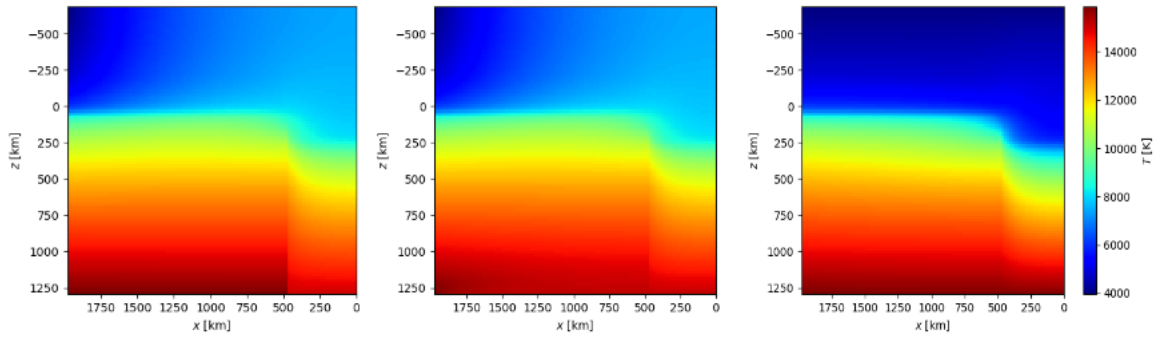

Figure 12: *Temperature distribution with different bottom boundary conditions set up. From left to right: different bottom boundary for each component and top boundary set to achieve* $\partial T/\partial z = 0$*, unique bottom boundary condition and top boundary set to achieve* $\partial T/\partial z = 0$*, top and bottom boundary conditions set to the respective points of the left boundary condition, Eq.* (32)*.*

that the density, the opacity and the source function are all approximated by a linear function at the local segment. At the bottom of the atmosphere it is necessary to specify boundary condition to initiate the integration. As the bottom boundary is deep below the surface, I set it to $I(\tau_0) \equiv B(\tau_0)$.

Our snapshot is two-dimensional, but we solve the RTE in 1.5-dimensional approach where the snapshots is sampled along linear rays. At disk center every vertical column in the model is sampled by one ray and $\mathrm{d}s \equiv \mathrm{d}z$. Away from disk center, at heliocentric angle θ ($\mu = \cos\theta$, at disk center $\theta = 0 \Rightarrow \mu = 1$, towards the limb $\theta \to \pi/2 \Rightarrow \mu \to 0$), $\mathrm{d}s \equiv \mathrm{d}z/\mu$, and we interpolated the values of the temperature and the pressure from the model to a slanted grid. Then we compute the opacity using the new interpolated values of T and p and integrate the optical depth along each of the slanted rays.

5 Results

5.1 Preliminary experiments (failed solutions)

To reach the proper setup of the system we made several experiments. One of the unknowns of this model were the proper top and bottom boundary conditions of the temperature distribution. From the Spruit's paper we know Eqs. (32) and (33), these equations made us wonder if the boundaries have to be defined different inside and outside the tube.
Our first attempt was to use different conditions for inside and outside, using bottom-point of the initial guess to the bottom horizontal ghost zones and copying the top-points of the domain to the top ghost zone to achieve $\partial T/\partial z = 0$ at the upper atmosphere.

We expect the upper atmosphere to be homogeneous and, from left-hand panel in Fig. 12 we see that it is not being fulfilled. It's cooler at the quiet Sun and the bottom is neither homogeneous.
The next experiment consisted on setting the same bottom boundary condition to all the domain, without differentiating between the two components. We used the initial guess inside the tube at the bottom for all the horizontal ghost zone.
In the central panel at Fig. 12 we can observe that the upper atmosphere remains not ho-

mogeneous, and the bottom of the domain is still not enough satisfactory. Noticing that the distribution at the cool component is not fitting with the left boundary, we finally defined them homogeneous for both top and bottom using the respective points of the left boundary condition, Eq. (32). From right-hand panel in Fig. 12 we can see how the temperature is homogeneous and smooth for the entire domain.

Another test we made was to analyze the three numerical schemes mentioned through Section 3: Jacobi, Gauss-Seidel and successive overrelaxation; to select the best one for our model (see Fig. 22 in the Appendix). The Jacobi method is the slowest one and SOR is the fastest one, as it is expected. All methods reach the acceptance error we defined (10^{-6}) in less than 6000 iterations and the solutions reached are the same. Although SOR method is the fastest one, we used GS to compute all the solutions, the convergence of GS is also fast compared to Jacobi and it does not depend on the relaxation factor, ω.

5.2 Model E as the showcase of a "pore"

In the original Spruit constructed 12 models with characteristics specified in Table 1, the temperature distribution of these models solved with our method is shown in the Appendix Figs. 23 and 24. Six of these models are constructed with $z_w = 100$ km and six with $z_w = 200$ km. In each of the two groups, the radius of the tube is varied from around 100 to around 500 km and with q in the range from 0.221 for the smallest tube to 0.161 for the largest one. In this section we will focus in depth on our model E (Table 2) characterised by a tube radius of 500 km, a Wilson depression of 200 km and the heating attenuating factor is set to 0.2. This setup is very similar to Spruit's model 12. The result of the temperature variation with distance from the axis at several depth are given in the right-hand panel of Fig. 4 of the original paper. The left-hand panel of the same figure shows the results for model 1, the smallest and the shallowest tube which is close to our model A*. We first focus on the model E because the match to Spruit's result is reasonably good. Later on, in Sect. 5.4 we will briefly return to the case of the model A* and the differences in respect to the original results, and in Sect. 5.3 we will discuss a sequence of models with varying radius of flux tube (our models A-E equivalent to Spruit's 7-12). The values of the input parameters that define each model are: the Wilson depression $z_w = 100$ km and $z_w = 200$ km , the efficiency factor for the vertical heat transport q and the radius of the tube r_0 in km and r_{grid} in km for the corresponding radius adapted to the horizontal grid d_x of the domain, see Tables 1 and 2.

To compare our results with the ones from Spruit's we took the Fig. 4 from his paper (Spruit, 1976), see Fig. 13. We cannot expect them to fit perfectly due to the initial guess of our model is not the same as Spruit's. Notice that his results have a drop at the wall. This drop is probably artificially introduced from the results of the computation due to the wall having two different values of temperature for the same x. We can also see the effect of the ΔT implementation above the surface in our model, appears a "moustache" shape. This effect is caused by the fact that we fixed the temperature at the wall by $\Delta T + T^{in}_{initial}$ and it is lower than the temperature reached above the surface. This artefact from the wall definition shows that the wall is not perfectly defined. ΔT depends on the horizontal Nusselt number, and it is related to the diffusion coefficients. Remember that we fixed the values of K^{rad} above the surface, and probably this artefact is also caused by this fix. However, note that the model 12 fits pretty well the Spruit's one.

To see the effect of the wall definition we compare the temperature distribution of model E with and without the wall method (Fig. 30 in the Appendix). Notice that as the height gets

Model	q	z_w [km]	r_0 [km]	$r_{\rm grid}$ [km]	d_x [km]
1	0.221	100	84	80	5
2	0.209	100	114	110	5
3	0.199	100	157	155	5
4	0.190	100	217	210	10
5	0.181	100	311	300	15
6	0.171	100	473	460	20
7	0.221	200	83	80	5
8	0.205	200	115	115	5
9	0.192	200	157	155	5
10	0.181	200	220	220	10
11	0.171	200	315	315	15
12	0.161	200	473	460	20

Table 1: *Characteristics of the* 12 *tube models, this values are taken from Spruit's paper (1976).*

Model	q	z_w	r_0 [km]	d_x [km]
A	0.2	200	100	5
B	0.2	200	200	10
C	0.2	200	300	15
D	0.2	200	400	20
E	0.2	200	500	20
A*	0.2	100	100	5
B*	0.2	100	200	10
C*	0.2	100	300	15
D*	0.2	100	400	20
E*	0.2	100	500	20

Table 2: *Characteristics of the tube models A-E and A*-E*.*

deeper ($z > 0$) the temperature at the quiet Sun for the model without the wall is cooler than the one with the wall. Moreover, for all heights the temperature inside the tube is higher for the model without the wall. This differences are caused because there is no restriction or treatment through the wall and the radiation can cross the wall and reach further into the centre of the tube, so the temperature outside the tube is cooler and inside is hotter.

As we described in Sect. 2.6 we computed pressure using the upper boundary pressure from the initial guess model as starting point p_0. p_0 is a free parameter and we have some freedom to choose it, we made some experimentation over it to look for the most stable result. We smoothed the transition between the cool and the hot component by using the three variants described in Fig. 10. The results of this variants are shown in Fig. 25 in the Appendix. For the variant 1 (left-hand panel in Fig. 25), we followed the method defined by Spruit in his paper, to find p_0 iteratively to have $\tau(z_w) = 1$. We don't know exactly which is this height and we make the false assumption that $\tau = 1$ at every point inside the tube at the same geometrical height, assuming the wall is vertical and the tube is flat. Spruit does it only in the axis of the tube, but we made it for all the columns. We can see how the isobars maintain the shape of p_0 shown in Fig. 10 with the vertical drop at the wall and inside the tube grows (more prominent in deeper layers) until it reaches a point where becomes stationary.

For the variant 2 the p_0 is set equal to the value at the top for the initial model outside the

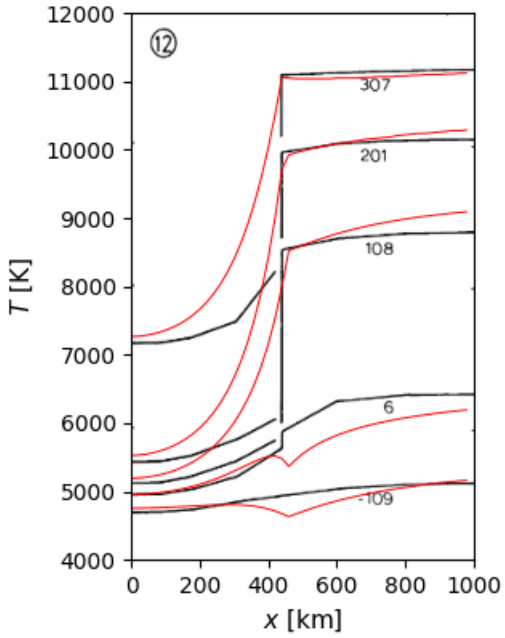

Figure 13: *Temperature at several depths for model 12 (Table 1), red lines, compared with Spruit's Fig. 4 (1976), black lines.*

tube and to the shifted value at the axis of the tube. The transition between the value at the hot component and the value at the axis of the tube has been smoothed gradually. The resulting pressure is as smooth as the pressure settled at the top boundary of the domain (central panel in Fig. 25). Finally, variant 3 is a combination of variants 1 and 2. The value of p_0 outside the tube is set as in the variant 2, but inside the tube the shifted value is fixed for the first 300 km from the axis outwards, and then gradually smoothed for the first 200 km from the wall inwards. As this variant is a combination of variants 1 and 2, the resulting pressure is also a combination of the previous results (right-hand panel in Fig. 25). We can see how the transition of the wall is smoothed and in the deeper layers the pressure gradually increases until it reaches a point where pressure becomes stationary. As we move to higher layers in the atmosphere, the growth of the pressure next to the wall inside the tube disappears and, after the smoothing, the pressure becomes stationary. If the tube is narrow, variant 2 and 3 are almost identical. By setting the integration constant of pressure we are mimicking the effect of magnetic field. As variant 3 has an additional free parameter and variant 2 is gradually decreasing, the lack of the additional free parameter led us to use variant 2 for the following steps.

The resulting density, opacity and optical depth based on the three variants can be seen in Figs. 26, 27 and 28.

5.3 Variation of the model E

To study deeply the effect of the radiative transfer through the wall we vary the model E by making the tube gradually narrower and shallower (see Table 2 and Fig. 29 in the Appendix for the temperature distribution). In this section we will analyze the effect of the different parameters over the temperature.

In the Fig. 14 we plotted the deviation of the temperature at the axis of the tube from the initial guess to analyze how the radius of the tube affects the temperature. We can see how the

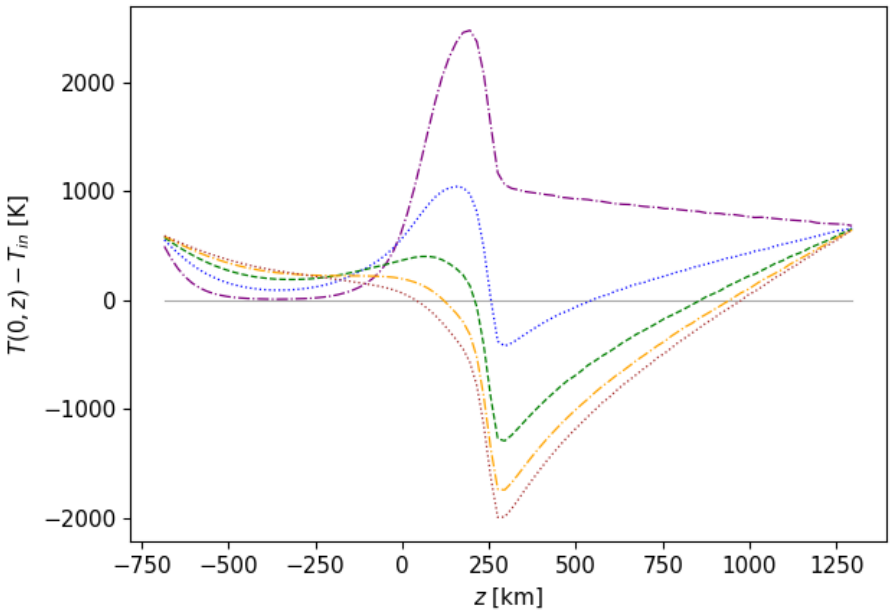

Figure 14: *Deviation from the initial temperature inside the tube ($T(0,z) - T^{in}$) for models A-E (Table 2). Purple line (dash-dotted) the model A, blue line (dotted) for model B, green line (dashed) for model C, orange line (dash-dotted) for model D and brown line (dotted) for model E, the solid grey line is plotted for reference ($T(0,z) - T^{in} = 0$).*

narrowest tube (model A) is heated the most and the deviation have a similar shape to ΔT (Fig. 8b). As the radius gets wider the tube is less heated, even in the widest tubes the temperature around $z = 230$ km, at the peak of ΔT, gets hotter than the initial guess. At the deepest heights, cooling for the wider tubes is due to the radiation from the hotter component being unable to reach the centre of the tube.

Another representative plot of the effect of the radius on the temperature at the axis of the tube can be seen in Fig. 15. This figure shows the temperature at several heights for the models A (red), C (blue), E (green), the models have been shifted to match the wall. In this plot we can see that at the same distance of the wall, the thinnest tube is more heated. This result is expected, because of our vertical boundary condition inside the tube. The tube is heated by radiation horizontally from both sides, imagine a symmetric tube, i.e. with two walls, both walls are heating inversely proportional to the distance from the walls, as the distance from the wall inwards increase, the heating decreases.

Other parameter to analyze is the Wilson depression. We computed models A-E modifying z_w to 100 km (models A*-E*). In the Fig. 31 in the Appendix we can see how the temperature in the horizontal direction changes with $z_w = 200$ km (black) and $z_w = 100$ km (red). Notice the "moustache" shape over the surface for the models with $z_w = 100$ km is not so pronounced in comparison with models having $z_w = 200$ km. This is a clear effect of the Wilson depression, as the temperature at the wall is closer to the initial guess in both components for models with $z_w = 100$ km than the models with $z_w = 200$ km (the difference between the two components is lower).

In Fig. 16 we can see how the temperature at the axis of the tube changes with radius at $z = 115$ km and $z = 315$ km for models defined in Table 2. Note that at deeper layers (dashed line), the tubes with $z_w = 100$ km (red) are hotter than the tubes with $z_w = 200$ km (blue). The thinnest

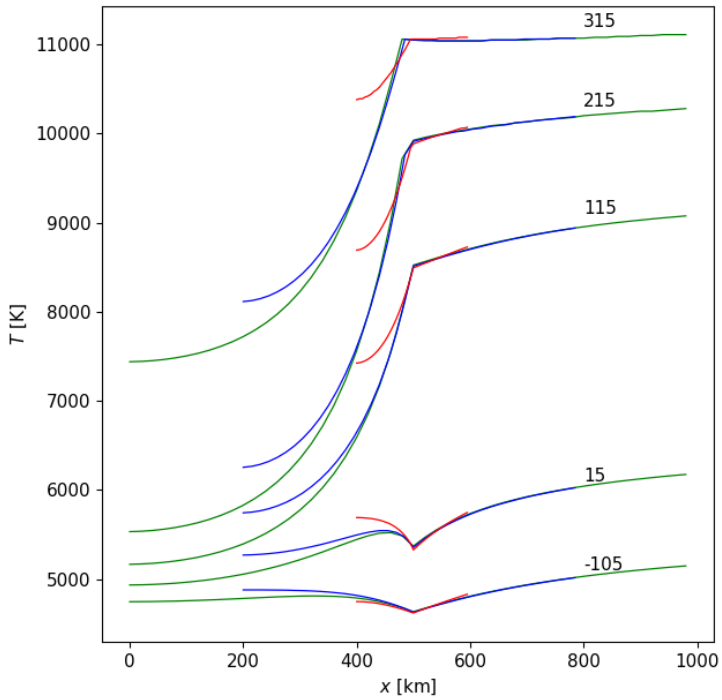

Figure 15: *Temperature at several depths (indicated at the curves, in km), red line for model A, blue line for model C and green line for model E (Table 2). The models are shifted to match the wall.*

tube models give nearly the same temperature at the axis for both initial Wilson depressions at both heights (pairs of left-most points in Fig. 16). The bigger the flux tube is, the more influence has the initial Wilson depression in the deeper layers where ΔT is the largest, but not at the surface where both pairs of curves remain similar.

In the same direction as the analysis of Fig. 14, we can plot the deviation from the initial guess at the axis of the tube for the models in Table 2. Fig. 17 shows how the temperature on the tube axis at $z = 255$ km, where the peak of ΔT is approximately located, has deviated from the initial guess for each model. It seems clear that for the shallower tubes the temperature reached at the axis of the tube is cooler than the initial one regardless of the radius. On the other hand, the deeper tubes have a similar behaviour, if we refer to the shape of this plot, but in the narrower tubes the temperature at the axis is hotter than the initial one. Around $r_0 \approx 200$ km the temperature is almost the same and as the radius increases, the temperature gets cooler than the initial one. Note that both Figs. 16 and 17 have a similar decreasing shape. We can see how the narrowest tube is more heated due to radiation from the hotter component than the widest one. As the tube is wider, the heating at the axis is reduced because the radiation can not reach the axis of the tube. This effect is represented in both figures with the fitting curve shape. It is expected that for wider tubes, the curve fitting the points in the Fig. 17 reaches a certain convergence at some radius and become flat.

Figure 3b from Spruit's paper (1976) shows the temperature on the axis of tubes $1, 6, 7$ and 12. We made the same plot for models A, E, A* and E*, see Fig. 18. In Spruit's Figure we can see how the temperature above the surface for the thinnest tubes $(1, 7)$ exceeds the

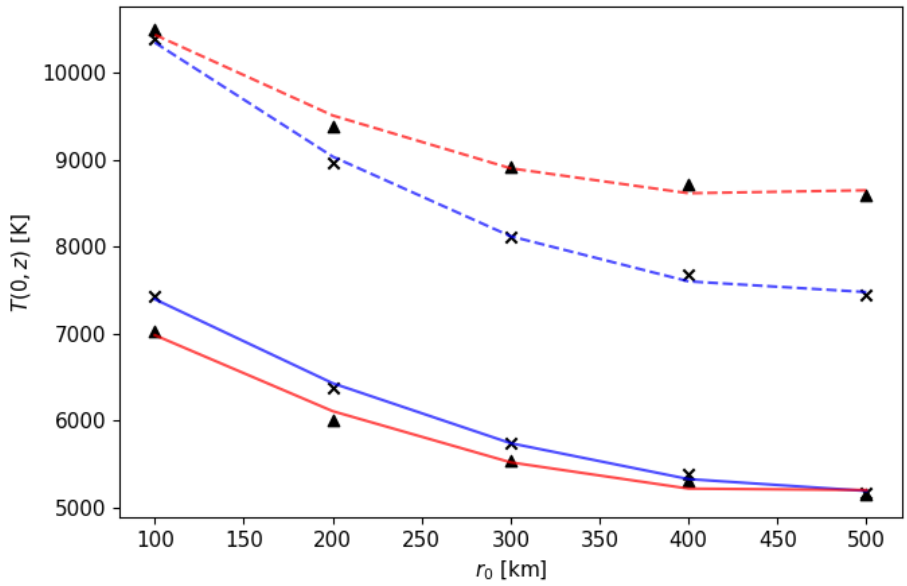

Figure 16: *Temperature at the axis of the tube for models A-E × (blue), and models A*-E*, ▲ (red), at $z = 115$ km (solid) and $z = 315$ km (dashed) fitting a grade 2 polynomial curve (Table 2).*

temperature at the quiet sun. This effect does not appear in our model, instead, we can see how the temperature inside the tube of our models converge at $z \approx -300$ km, except for the model A, which converges at higher height (see Fig. 14). This differences are probably caused by the definition of the boundary condition at the top of the domain. Another characteristic that is observed in Spruit figure is the heights where the temperature profiles cross for each tube radius. In his Figure, the temperature profiles of the wider tubes cross each other at higher heights (closer to the surface), and the narrower tubes cross deeper below the surface, both crossings take place between $z = 100$ km and $z = 200$km. In contrast, in our Figure we can see that the temperature profiles of narrower tubes cross three times, one at $z \approx 50$ km, one between $z = 100$ km and $z = 200$ km and one at $z \approx 350$ km. In the interval where Spruit's temperature profiles cross, we can see the same behaviour in our models. The main difference is that, as we said, the temperature profiles of our narrower tubes cross three times. We can not know if the third cross for the narrower tubes (the one at $z \approx 350$ km) is also in his models, the temperature axis of Spruit's Figure is constrained for $T < 9.5 \cdot 10^3$ K. In his figure we can also see that the temperature profiles of models 6 and 7 get very close between $z = 200$ km and $z = 300$ km, models A and E* in our case. This feature is not seen in our figure (Fig. 18), at this interval the temperature profiles of the models in question have a difference of around 1500 K. Note that for the thinnest tube, the comparison with Spruit's results is not pretty good. We will discuss the differences in the Sect. 5.4. On contrary to thinnest tubes, the profiles of the wider tubes fits reasonably well, as we have seen in Fig. 13. As we mentioned before, we didn't use the same initial model as Spruit's and we don't know exactly how he defined the wall transition. These reasons, in addition to how the diffusion coefficients are computed cause differences between his results and ours. As we will see in Sect. 5.4, the thinnest tube is the model more affected by this differences. In a qualitative way, we can affirm that our model reproduces Spruit's results

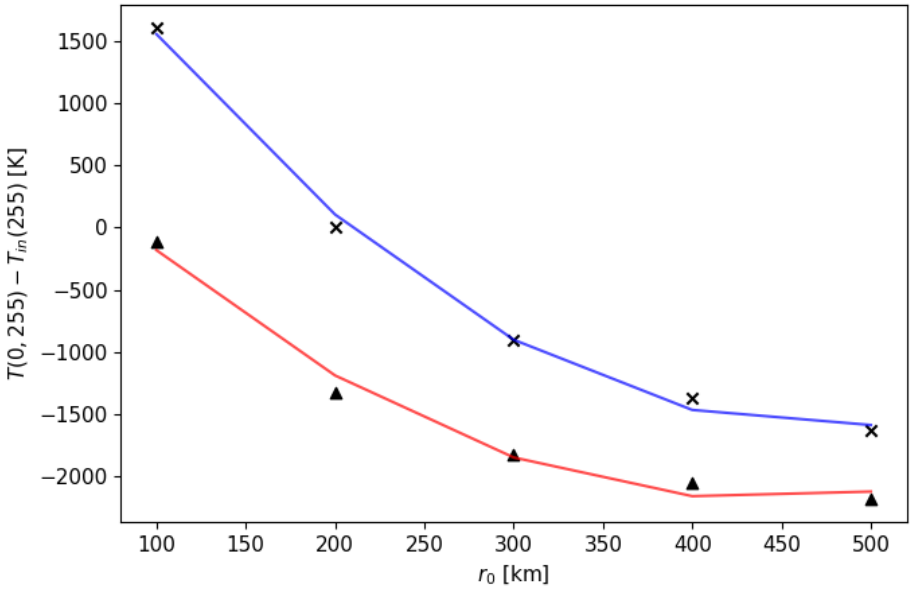

Figure 17: *Deviation from the initial temperature inside the tube ($T(0,z) - T^{in}$) for models A-E with $z_w = 200$ km, ×, and models A^*-E^* with $z_w = 100$ km, ▲, at $z = 255$ km fitting a grade 2 polynomial curve (Table 2).*

reasonably good.

Another important parameter is the attenuating factor q. In Fig. 19 we represented the model E with different values of q: 0.1 (red), 0.2 (black) and 0.4 (blue). We can see how as the value of q increases, the temperature inside the tube also increases due to the vertical convective energy transport increases. This is an expected result based on the definition of the vertical convective coefficient. With larger value of q the vertical convective transfer of energy is more effective and the temperature inside the tube increases more significantly than with a smaller attenuating factor. We don't really know the exact value of q and we should estimate it from realistic 3D simulations, but for this analysis we will use the same range of values as Spruit.

5.4 Discrepancies in model 1

On contrary to model 12, model 1 does not fit pretty well with Spruit's results (see Fig. 20). We can see how our models shows a smooth transition between the two components. This smooth transition is due to the radius being comparable to the distance at which the radiation heating reaches the interior of the tube. Note that the interior of the tube is being heated by the two walls of the tube, boundary condition at the axis is symmetric, Eq. (35). In Spruit's results, we can see the vertical drop at the wall, also present in model 12, Fig. 13. As we mentioned in the discussion of model 12, this drop is difficult to understand and would require a extremely fine grid or two different temperatures at the same distance of the axis, at the wall. We don't know the grid used by him and neither how he computed the transition zone precisely.

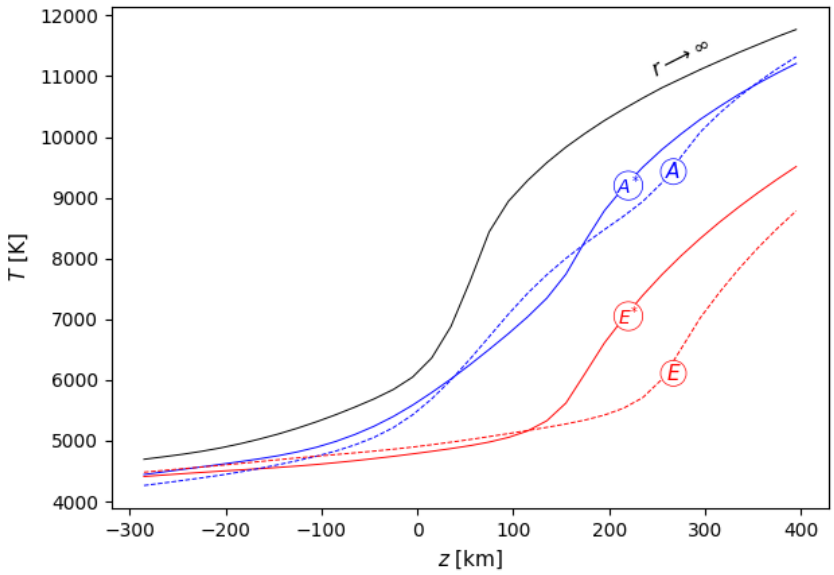

Figure 18: *Temperature at the axis of the tube, for models A, E, A*, E* (Table 2). Black line (solid) represents the temperature at the quiet sun.*

5.5 Spruit's model vs. realistic 3D MHD simulation

Numerical 3D simulations are one of the principal tools to analyze dynamics of the solar and stellar atmospheres. The early development of these simulations (Nordlund, 1982) was motivated by the need to understand spatially resolved process on the solar surface. Here we describe a snapshot from a simulation performed with the MURaM code (Vögler, Shelyag, et al., 2005) with initial the vertical magnetic field of 200 G (Vitas et al., 2009) representing a small portion of a solar plage region. This particular simulation was analyzed in great detail by Cubas Armas (2015). The size of the simulation domain was 6 Mm × 6 Mm in the horizontal plane (288 × 288 grid points), and 1.4 Mm in the vertical direction (sampled by 100 grid points of which 1/3 is above the $\tau = 1$ surface).

The color map in Fig. 32 (in the Appendix) shows the continuum intensity at 500 nm computed from this snapshot[8]. The surface in the simulation is around 65 ×14 km above the bottom boundary[9]. The white contours in Fig. 32 show the distribution of the vertical magnetic field at fixed geometrical height ≈ 200 km below the mean surface. By looking for the brightening in the intensity map and the contours of the magnetic field we can identify small magnetic elements in the snapshot. We will focus on the element at $(X, Y) \approx (2.2, 4.8)$ Mm. In Figs. 33, 34 and 35 (in the Appendix) we zoom into this element and display the physical quantities at three geometrical heights (200 km below the mean surface, the mean surface and 280 km above it) at its location: the temperature and the pressure in the first row, the density and the vertical magnetic field in the second, and the opacity and the optical depth in the bottom row. The contours show the magnetic field below the surface (and they are well aligned with the magnetic field map in Fig. 33). At the location of the strong magnetic field, we see that all

[8]The specific intensity is computed using a simple spectrum synthesis code written IDL accounting for the major continuum opacity contributors like H^- bound-free and free-free absorption (Vitas, 2024, private communication).

[9]In a simplistic point of view, the snapshot in Fig. 32 is 65 points above the bottom of the domain, where $\tau \approx 1$.

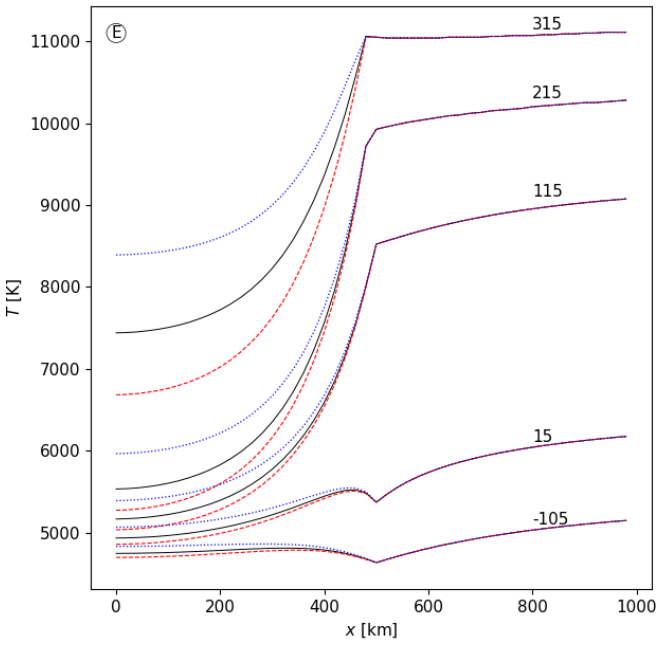

Figure 19: *Temperature at several depths (indicated at the curves in km) of model E (black line, $q = 0.2$), red-dashed line represent the same model modifying $q = 0.1$ and blue-dotted line modifying $q = 0.4$ (Table 2).*

other physical parameters are significantly reduced at the surface and 200 km below it. In Fig. 35 the temperature in the tube and the surrounding dark-lane is higher than in the photosphere and, as a consequence, the opacity contrast between the element and the photosphere is reduced. It is important to notice that not all magnetic fields in this snapshot cause surface brightenings and that not all surface brightenings are due the magnetic fields.

In Fig. 36 in the Appendix, we compare the vertical stratification of the temperature, the density, the pressure and the opacity in the two vertical columns identified as magnetic element and photosphere in Figs. 33-34, with the structure of these quantities in our model E, along the axis and in the unperturbed photosphere. The simulated photosphere is fairly similar to our unperturbed model in all quantities (blue pairs of curves). The simulated atmosphere is just one column from the 3D domain, while our quiet Sun column is similar to the initial model atmosphere, and therefore to the HSRA model atmosphere that we used to construct it. The vertical stratification in 3D snapshots show many sharp gradients in physical quantities (like T, p or ρ) that are smoothed out when the 3D snapshot is averaged over iso-tau surfaces into a 1D model. Our simulation is essentially a 2D modification of 1D models, so there is no physical mechanism in it to reproduce sharp gradients present in the real sun or in the realistic simulations. The structure within the magnetic element differs more. The 3D simulated element has higher temperature in the photosphere which is expected as we are comparing it against our model E which represents a wider fluxtube. The difference in the pressure and density, increasing from the mid-atmosphere downward, is likely due to the way we compute the pressure from the temperature, but also due to specifics of the model E. In any case, having in mind how different are two modeling approaches, the results in Fig. 36 are surprisingly similar which gives an additional confidence in our implementation of Spruit's modeling approach.

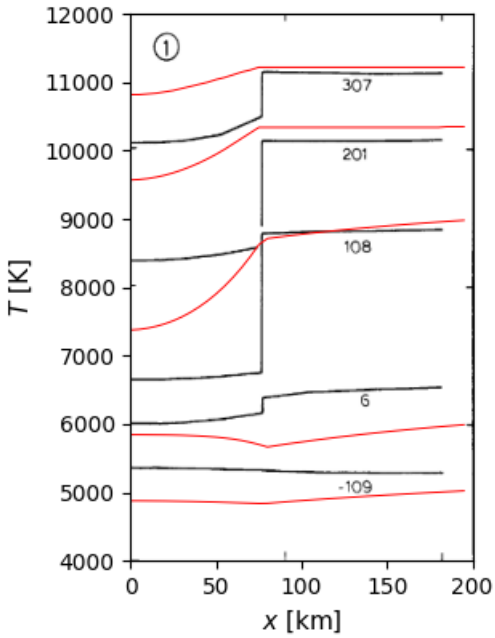

Figure 20: *Temperature at several depths for model 1 (Table 1), red lines, compared with Spruit's Fig. 4 (Spruit, 1976), black lines.*

5.6 Synthetic observations

Spruit (1976), defines the contrast of the brightness inside and outside of the tube as:

$$Q = \frac{I^{in}}{I^{out}} - 1 \tag{81}$$

From the original paper it is not entirely clear how the intensities were approximated. To compute the synthetic observations at disk center from our models A to E, we first duplicate the models by mirroring them around the tube axis and then we solve the radiative transfer equation following the method described in Sect. 4. The results of the intensity computed at 500 nm and normalized to the value in the unperturbed atmosphere are shown in Fig. 37 (in the Appendix). All the intensity profiles with the distance across the tube show the same W-like structure, with a spike of the intensity along the tube axis. The thinnest tube ($r = 100$ km) produces very high contrast in the center of the tube, $Q \approx 1.5$, which means that along the axis it is 2.5 times brighter than the photosphere. The constrast quickly drops with the radius of the tube. At $r = 300$ km, $Q \approx 0$, i.e. the tube is as bright as the photosphere. Finally, at $r = 500$ km, $Q \approx -0.5$, i.e. the tube is two times darker than the surrounding. This sequence replicates well the results of Spruit and it confirms his conclusion that the diameter of ≈ 600 km is the critical threshold for a magnetic tube to be dark or bright relative to the unperturbed granular cells. That conclusion is confirmed by observations (Keller et al., 1992).

It is interesting to note that the W-like shape is actually very similar to what the realistic numerical simulations predict, see Fig. 32. The bright magnetic elements are separated from the bright granules by darker material. While in the realistic simulations and in the nature this intensity profile is created by the magnetic field distribution, in our simulation its shape is controlled by the diffusion equation for the temperature and, equally important, by the distribution of the pressure and the way how the integration constant in the pressure computation is set up.

In Fig. 38 in the Appendix, we show the same intensity computations as in Fig. 37, but now convolved with a Gaussian function with FWHM of ≈ 0.3 arcsec (value of FWHM is chosen as in Spruit's paper, around 200 km). The profiles are smoothed as expected and the contrast is significantly reduced. The high-contrast peak in the thinnest tube is reduced to ≈ 0, which means that in the observations the smallest tubes would appear similarily bright as the unperturbed photosphere.

6 Discussion and Conclusions

In the thesis we revisited the seminal theoretical paper by Spruit (1976). In that work the author presented the first model of a magnetic flux tube embeded in the near-surface convection capable of explaining the variation in brightness of magnetic elements at the solar surface. Spruit's work consists in two parts. In the first part the energy equation is formulated as diffusion problem and solved. The solution is closed by the hydrostatic equation and equation of the ideal gas (equation of state). In the second part, the obtained thermal-pressure structure of the fluxtube model is used to derive the potential field distribution in magneto-hydrostatic equilibrium. In this thesis the focus is only on the former.

The reason for omitting the incorporation of the magnetic field is the very nature of Spruit's theory. In the real Sun and in the realistic simulations of the Sun the presence of the magnetic field concentration affects the fluid dynamics, reduces the heat transfer inside of a tube, reduces locally the pressure, the density and the continuum opacity, and it causes either enhancement or attenuation of the emergent intensity depending on the size of the tube. However, in Spruit's theory, the effects of the magnetic field are implicitly accounted through modification of the convective diffusion coefficient and the magnetic field is constructed to comply with already present thermodynamical structure. In that sense the nature of Spruit's theory is phenomenological. Still, it is capable to correctly predict relative contrast of magnetic elements at the solar surface.

There are various differences between our solution and the one from the original paper:

i We constructed the initial model (Sect. 2) following the directions given in the paper. As the exact model used by Spruit is not available, our initial model is not identical to the one used by Spruit. However, the solar mean 1D models are well defined and we do not expect significant effect on the results.

ii We solved the 2D diffusion equation using a combination of the 2-nd order finite-differences and the Gauss-Seidel method on the uniform Cartesian grid, while the original paper solves the problem using unspecified method in cylindrical coordinates.

iii We defined the temperature jump ΔT at the wall as it is defined by Spruit. The definition depends on the Nusselt number and on the related quantity η, the latter is the ration of the total and the radiative vertical diffusivity. Above the surface where the radiation dominates, these quantities quickly become ill-defined and some clipping is necessary, see our Fig. 3. Our approach is described in Sect. 2.2. Some differences in respect to Spruit's original work are likely. The different approach likely results in the moustache shape of the horizontal temperature cuts above the visible surface in our models (Fig. 13, Fig. 30, Fig. 15 and Fig. 31) and absent from equivalent figures in Spruit (1976). However, the appearance or absence of the moustache may simply be an effect due to the grid resolution.

iv The original paper is short of details of implementation of ΔT in the solution, saying only that "we absorb the steep gradient into a *jump* ΔT at the wall". Our implementation is described in Sect. 2.3. The implementation of ΔT certainly has a major effect on the model. In Fig. 30, we compared the models computed with and without the wall. The model with wall has obviously much sharper transition in temperature on the the interface between the tube and the unperturbed granule. It is expected as in our interpretation ΔT behaves as an additional, internal, boundary condition between the two regimes. The comparison between our model E and Spruit's model 12 , our Fig. 13, his Fig. 1, shows very similar behaviour giving an impression that we implemented ΔT in a similar way. However, there is an obvious difference between our model A* and his model 1, see Fig. 20. In this thin tube, our model shows a smooth transition in temperature which is a consequence of (a) radius of the tube being comparable to the distance at which radiation effective heats the interior of the tube, and of (b) the interior of the tube being heated from both walls (left and right, because the boundary condition at the axis is symmetric in temperature). On the other hand, Spruit's model shows nearly vertical drop of temperature even in this model. It is difficult to understand how is this solution even possible as it would required either extremely fine grid at the location of the wall (which seems unlikely although the exact grid is not known) or coexistence of two different temperatures at the same (x, z) coordinate. Therefore, the question of the ΔT implementation remains open.

v Spruit (1976) computed the variation of the intensity contrast across the solar disk (so-called "center-to-limb" variation, CLV). We repeated the same computation using our model and the preliminary results reproduce the observed behaviour. However, we leave for the future the direct comparison between CLV's. The reasons are: (1) our tube is better numerucally resolved than the one presented by Spruit and the radiation emerging from a slanted tube is more difficult to interpret; and (2) we solve the radiative transfer equation by trancing the rays which introduces additional numerical issues at the discontinuity created by the steep temperature gradient at the vertical hot wall that becomes increasingly exposed closer to the solar/stellar limb.

In Sect. 3 we reproduced the thermodynamic part of Spruit's paper using our own numerical approach to solving the diffusion equation. The results shown in Sect. 5.6 confirm that this simple model is capable predicting that the critical flux-tube radius at which the magnetic elements change from dark to bright is around 300 km. How universal is this result and can it be applied to other stars? Spruit (1976) limited its study to the Sun only. What is solar-specific in that model that we reproduced here? the direct comparison between CLV's

i The initial 1D model atmosphere is made out of a semi-empirical model for the Sun. Models for other stars are almost exlusively theoretical. Some grids of stellar models are publically available (for example the Castelli/Kurucz grid [10] or can be computed using open-source codes (e.g. the Tlusty code by Hubeny[11]. In any case the 1D model is used not only to set the initial atmosphere, but also to define the vertical boundary in the unperturbed component and both the top and the bottom horizontal boundaries. To specify a 1D model for a star, we need to specify its effective temperature T_{eff}, surface gravity g and metalicity or chemical composition.

[10] `http://kurucz.harvard.edu/grids.html`
[11] `https://www.as.arizona.edu/~hubeny/pub/`

ii The radiative diffusion coefficient (Eq. 6) includes a term κ which stands for the Rosseland opacity. To evaluate it we used a lookup table precomputed for the solar chemical composition. Therefore, the same table can be used for other stars if their T and p are in the range of the axes of the lookup table and as long as they have the solar composition. For a star of different composition the lookup table must be recomputed.

iii The convective diffusion coefficient includes the mixing length $\lambda = a_{MLT} \times H_p$ where a_{MLT} is dimensionless coefficient that is in the range between 1 and 2 for any star, and H_p is the pressure scale height which depends on the surface gravity ($= p/(\rho g)$) and, thus, on the stellar type. The smaller the star is, the higher is the gravity at the surface, the shorter is the pressure scale height. The typical turbulent velocity v (in Eq. (7)) weakly depends on the stellar type. Finally, the heat capacity at the constant pressure c_p is given by the equation of state for a given plasma composition, and, therefore, its lookup table has to be recomputed for a star with different composition.

iv The pressure is obtained from the temperature assuming the hydrostatic equilibrium (Eq. 39), which again includes the surface gravity and the ideal gas law. The ideal gas law is not a very good approximation in the solar atmosphere, but it is acceptable as long as hydrogen does not ionize significantly, so roughly at the temperatures below 10 000 K. In other stars, especially the coolest ones, the equation of state becomes increasingly complicated due to the formation of molecules (for example, H_2, H_2O, etc). Therefore, to apply Spruit's model to other stars it would be important to substitute the ideal equation of state with the realistic one.

v For the mean molecular weight we adopt $\mu = const = 1.26$ which is good for the solar atmosphere, but not below the solar surface. And it will vary with the chemical composition of a star.

vi In the computation of the specific intensities, we use precomputed opacities at 500 nm. Although the tables are universal for one chemical composition, it should be noted that our table is precomputed for the solar modeling with the main contribution to the continuum opacity being the ionization of the negative hydrogen ion. Therefore the table lacks some processes that may be important in other stars (for example, the dissociation of molecules).

vii Finally, our models have three input parameters, the radius of the tube, the attenuating factor q and the Wilson depression, that are set to values in the range that is empirically known from the solar observations. For other stars we know neither of the two as it is impossible to observe their spatially-resolved surfaces. We can speculate that the typical radius of the tube may scale with the pressure scale height H_p. The Wilson depression is roughly determined by the pressure difference inside and outside of the tube:

$$\Delta p(z) = p^{out}(z) - p^{in}(z) = \frac{B^2(z)}{8\pi} \tag{82}$$

If one makes assumption that the field strength along the axis is of the same order of magnitude in other stars as in the Sun (approximately between 1 and 2 kG), then it may provide an order-of-magnitude estimate of Wilson depression for other stars. This assumption may not be very wrong as we know that the field strength along the axis of magnetic elements in the Sun does not vary much although their are may vary for orders of magnitude. However, rather than making wild guesses, one could use 3D realistic simulations to estimate what would be a typical Wilson depression in these stars.

Finally, we conclude that the results of Spruit (1976) are sufficiently reproducible in our implementation. The differences may be attributed to different interpretation of the model assumptions (especially the construction of the wall between the hot and cold component), to differences in the input data (initial model, opacities) and to different numerical methods. The ability of our version of the model to correctly predict the contrast of the solar magnetic elements gives us a confidence to apply this model to analytical modeling of magnetic elements in other stars. That remains as the next step in the future continuation of this research.

References

Afram, N. et al. (2011). "Intensity contrast from MHD simulations and HINODE observations". In: *Astronomy & Astrophysics* 526, A120.

Asplund, M. et al. (2009). "The chemical composition of the Sun". In: *Annual review of Astronomy & Astrophysics* 47, pp. 481–522.

Biermann, L. von (1941). "Der gegenwärtige stand der theorie konvektiver sonnenmodelle". In: *Vierteljahresschrift der Astronomischen Gesellschaft* 76, pp. 194–200.

Bond, J.W. et al. (1966). *Atomic Theory of Gas Dynamics*.

Cameron, R. (2009). "Solar surface magnetoconvection simulations: A brief review of solar dermatology". In: *Science in China Series G: Physics, Mechanics and Astronomy* 52, pp. 1665–1669.

Carlsson, M., De Pontieu, B., and Hansteen, V.H. (2019). "New view of the solar chromosphere". In: *Annual Review of Astronomy & Astrophysics* 57, pp. 189–226.

Cubas Armas, M. (2015). "Spectral diagnostics from three-dimensional magnetoconvection simulations of the solar photosphere". In: *Master thesis, University of La Laguna & Instituto de Astrofisica de Canarias*.

Deinzer, W. et al. (1984). "Model calculations of magnetic flux tubes. I-Equations and method. II-Stationary results for solar magnetic elements". In: *Astronomy & Astrophysics* 139, pp. 426–449.

Gingerich, O. et al. (1971). "The Harvard-Smithsonian reference atmosphere". In: *Solar Physics* 18, pp. 347–365.

Khomenko, E. and Collados, M. (2008). "Magnetohydrostatic sunspot models from deep subphotospheric to chromospheric layers". In: *The Astrophysical Journal* 689.2, p. 1379.

Keller, C.U., Stenflo, J.O., and Luhe, O. von der (1992). "High spatial resolution magnetograms of solar active regions". In: *Astronomy & Astrophysics* 254, p. 355.

Kurucz, R.L. (2014). "Model atmosphere codes: ATLAS12 and ATLAS9". In: *Determination of Atmospheric Parameters of B-, A-, F-and G-Type Stars: Lectures from the School of Spectroscopic Data Analyses*, pp. 39–51.

Norris, C.M., Beeck, B., et al. (2017). "Spectral variability of photospheric radiation due to faculae-I. The Sun and Sun-like stars". In: *Astronomy & Astrophysics* 605, A45.

Norris, C.M., Unruh, Y.C., et al. (2023). "Spectral variability of photospheric radiation due to faculae–II. Facular contrasts for cool main-sequence stars". In: *Monthly Notices of the Royal Astronomical Society* 524.1, pp. 1139–1155.

Nordlund, A. (1982). "Numerical simulations of the solar granulation. I-Basic equations and methods". In: *Astronomy & Astrophysics* 107, pp. 1–10.

Olson, G.L. and Kunasz, P.B. (1987). "Short characteristic solution of the non-LTE line transfer problem by operator perturbation—I. The one-dimensional planar slab". In: *Journal of Quantitative Spectroscopy and Radiative Transfer* 38.5, pp. 325–336.

Perdomo García, A. et al. (2023). "Opacity for realistic 3D MHD simulations of cool stellar atmospheres". In: *Astronomy & Astrophysics* 675, A160.

Pizzo, V.J. (1986). "Numerical solution of the magnetostatic equations for thick flux tubes, with application to sunspots, pores, and related structures". In: *Astrophysical Journal, Part 1* 302, pp. 785–808.

Pizzo, V.J., MacGregor, K.B., and Kunasz, P.B. (1993). "A numerical simulation of two-dimensional radiative equilibrium in magnetostatic flux tubes. II-Computational results". In: *Astrophysical Journal, Part 1* 413, pp. 764–777.

Solanki, S.K. (1993). "Small-scale solar magnetic fields: an overview". In: *Space Science Reviews* 63.1-2, pp. 1–188.

Spruit, H.C. (1974). "A model of the solar convection zone". In: *Solar Physics* 34, pp. 277–290.

— (1976). "Pressure equilibrium and energy balance of small photospheric fluxtubes". In: *Solar Physics* 50, pp. 269–295.

Stenflo, J.O. (1989). "Small-scale magnetic structures on the Sun". In: *The Astronomy and Astrophysics Review* 1, pp. 3–48.

Stix, M. (2004). *The sun: an introduction*. Springer Science & Business Media.

Schrijver, J. and Zwaan, C. (2008). *Solar and stellar magnetic activity*. Vol. 34. Cambridge University Press.

Vernazza, J.E., Avrett, E.H., and Loeser, R. (1973). "Structure of the solar chromosphere. Basic computations and summary of the results". In: *Astrophysical Journal* 184, pp. 605–632.

Varga, R.S. (2000). "Basic Iterative Methods and Comparison Theorems". In: *Matrix Iterative Analysis*. Springer Berlin Heidelberg, pp. 63–110.

Vitas, N. et al. (2009). "Explanation of the activity sensitivity of Mn I 5394.7 Å". In: *Astronomy & Astrophysics* 499.1, pp. 301–312.

Vögler, A., Shelyag, S., et al. (2005). "Simulations of magneto-convection in the solar photosphere-Equations, methods, and results of the MURaM code". In: *Astronomy & Astrophysics* 429.1, pp. 335–351.

Vögler, A. and Schüssler, M. (2007). "A solar surface dynamo". In: *Astronomy & Astrophysics* 465.3, pp. L43–L46.

A Appendix: Additional figures

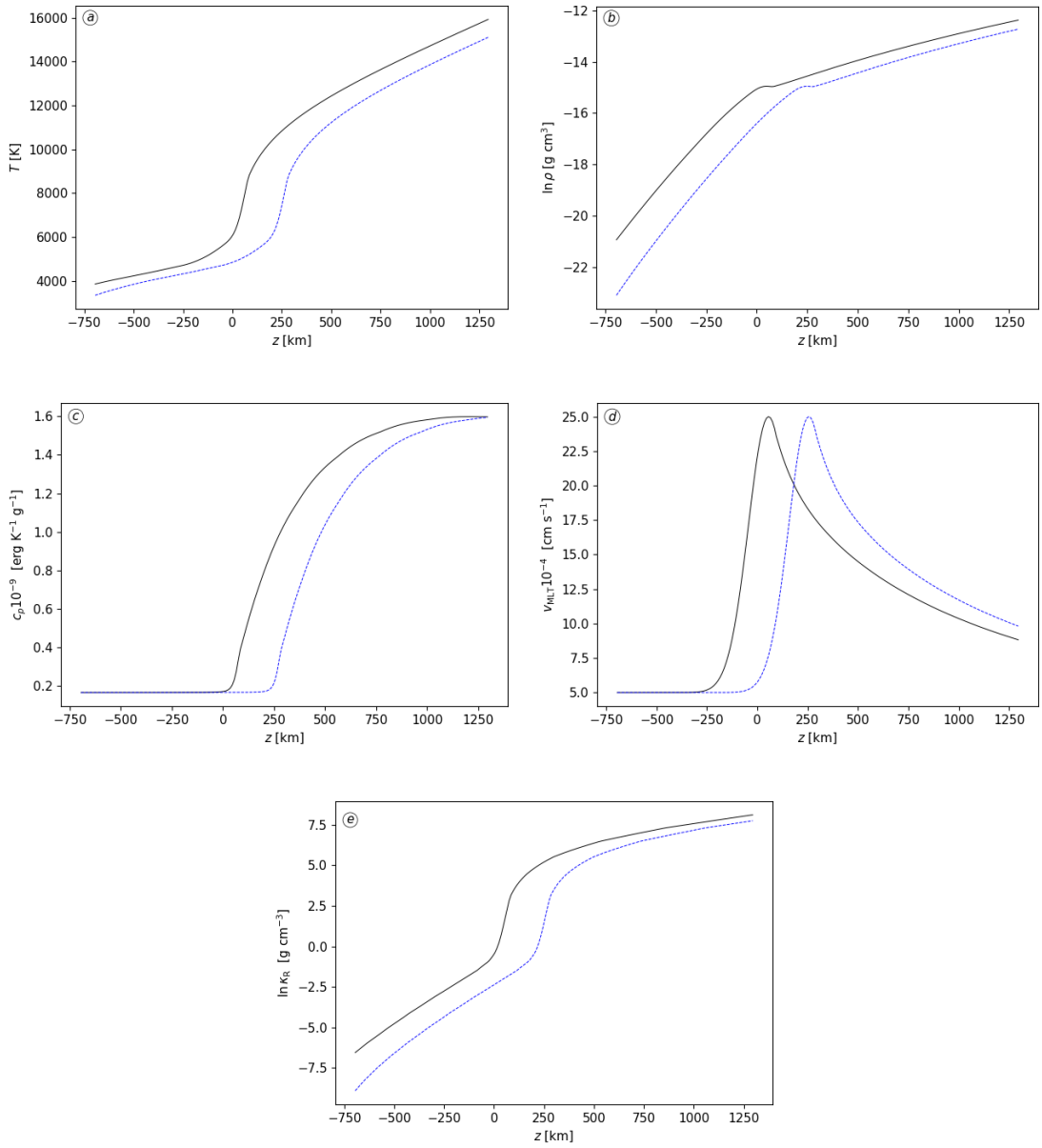

Figure 21: *Key quantites from the model atmosphere (Sect. 2.5) against the geometrical height: unperturbed atmosphere (black solid), fluxtube (blue dashed). Both models are shown agains the height scale of the unperturbed one. (a) The temperature T, (b) the density ρ, (c) the specific heat capacity at constant pressure c_p, (d) the convection (or turbulent) velocity v_{MLT} and (e) the Rosseland opacity κ_{R}.*

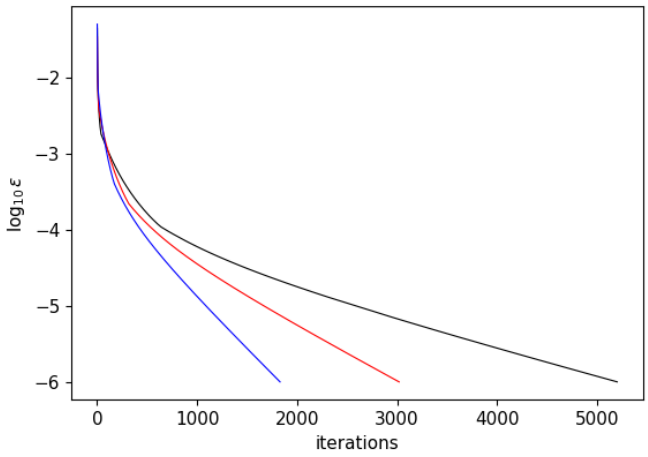

Figure 22: $\log_{10} \varepsilon$ *(error) versus iterations for each method: Jacobi (black), Gauss-Seidel with* $\omega = 1.3$ *(red) and successive overrelaxation (blue).*

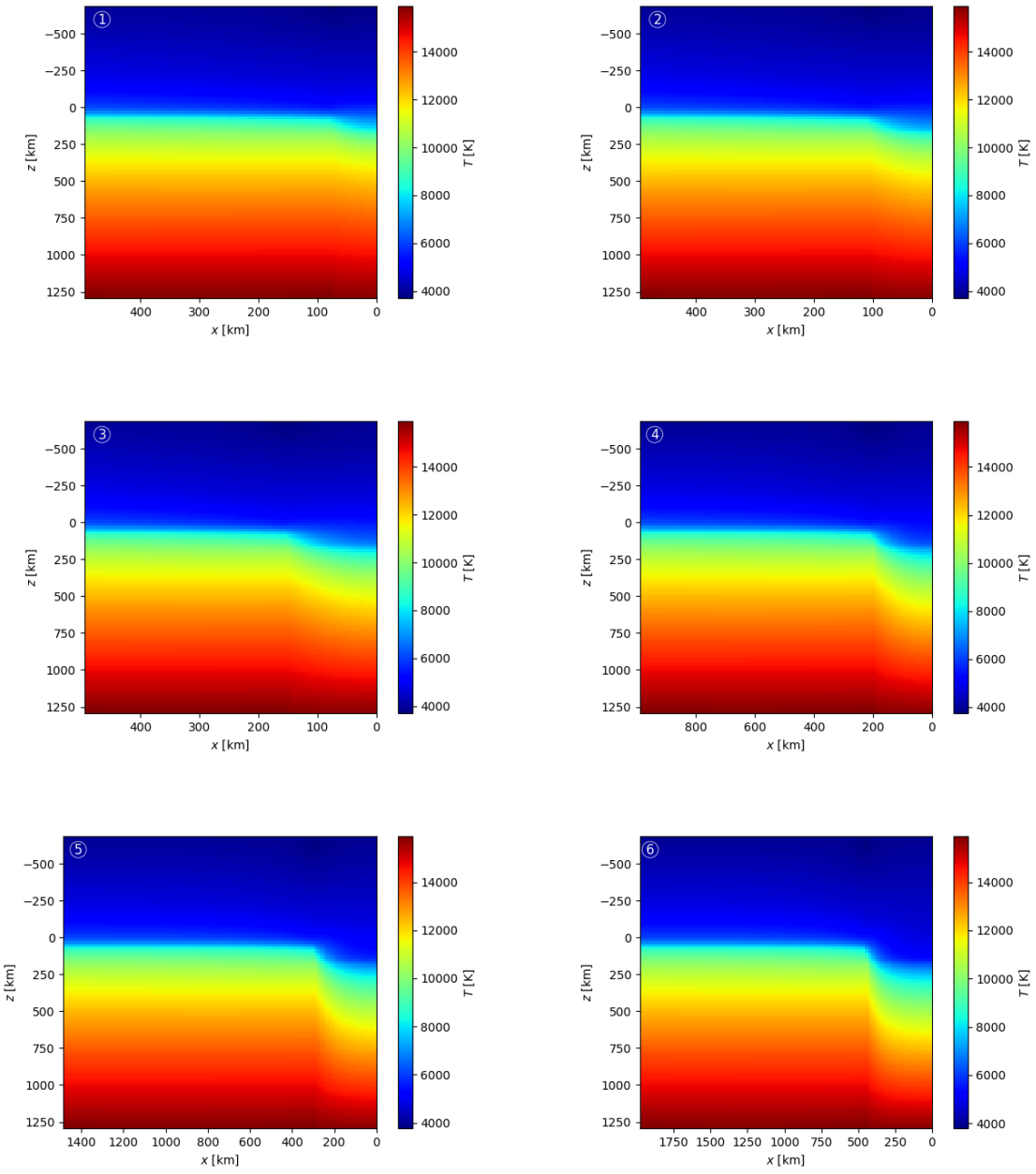

Figure 23: *Temperature distribution of models 1-6. (Table 1)*

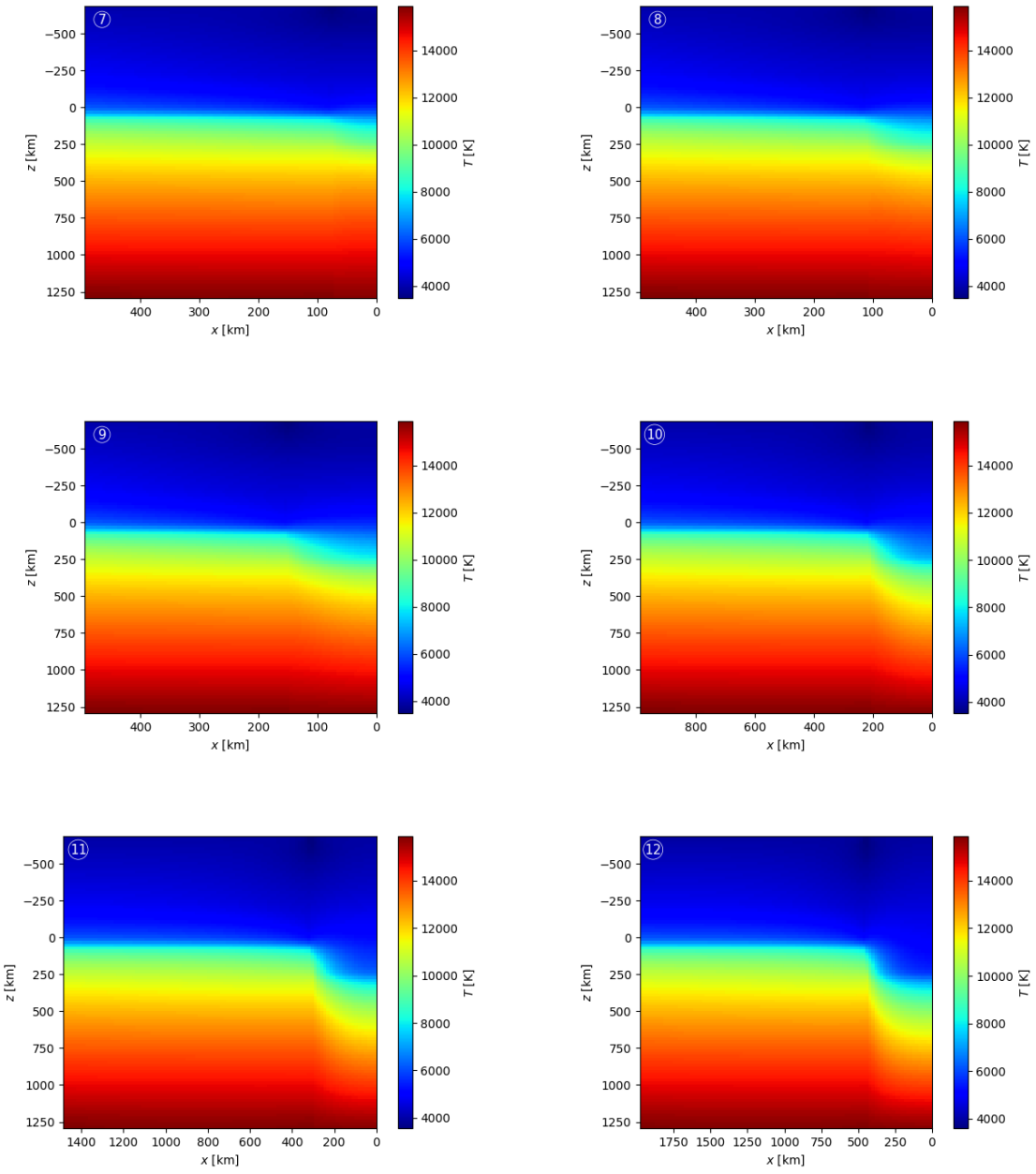

Figure 24: *Temperature distribution of models 7-12. (Table 1)*

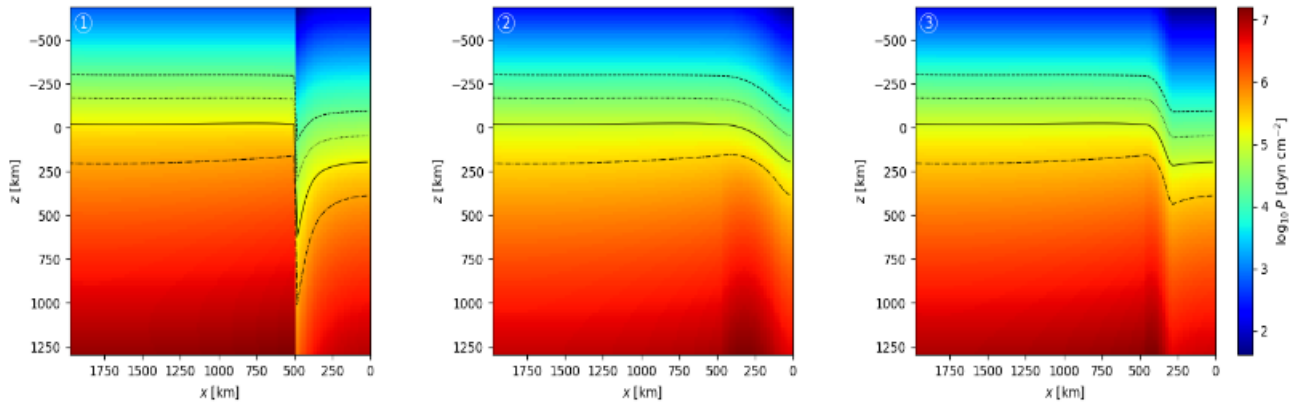

Figure 25: *Pressure distribution with different treatment for the transition zone. From left to right: variants 1, 2, 3 of p_0, see Fig. 10. Isobars at 10^4 (dashed line), $10^{4.5}$ (dotted line), 10^5 (solid line), $10^{5.5}$ (dash-dotted line) dyn* cm^{-2}.

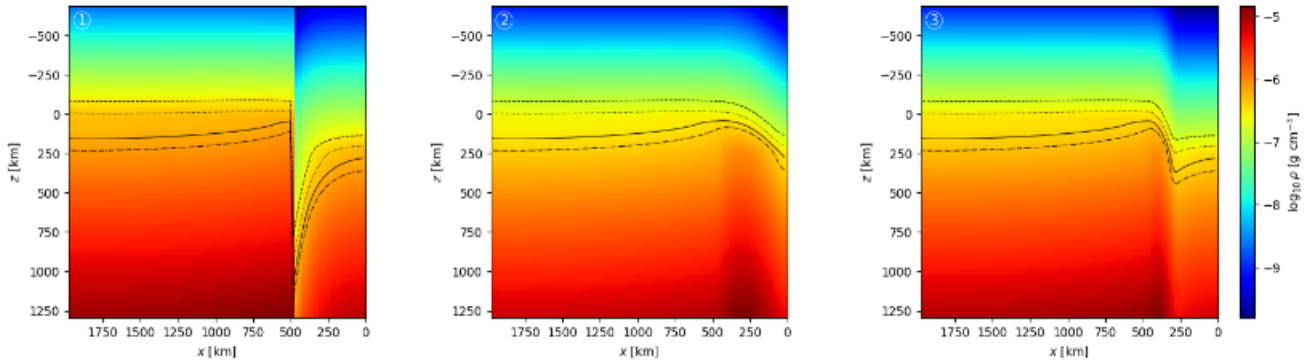

Figure 26: *Density distribution with different treatment for the transition zone. From left to right: variants 1, 2, 3 of p_0, see Figure 10. Isobars at $10^{-6.75}$ (dashed line), $10^{-6.55}$ (dotted line), $10^{-6.4}$ (solid line), $10^{-6.3}$ (dash-dotted line) g* cm^{-3}.

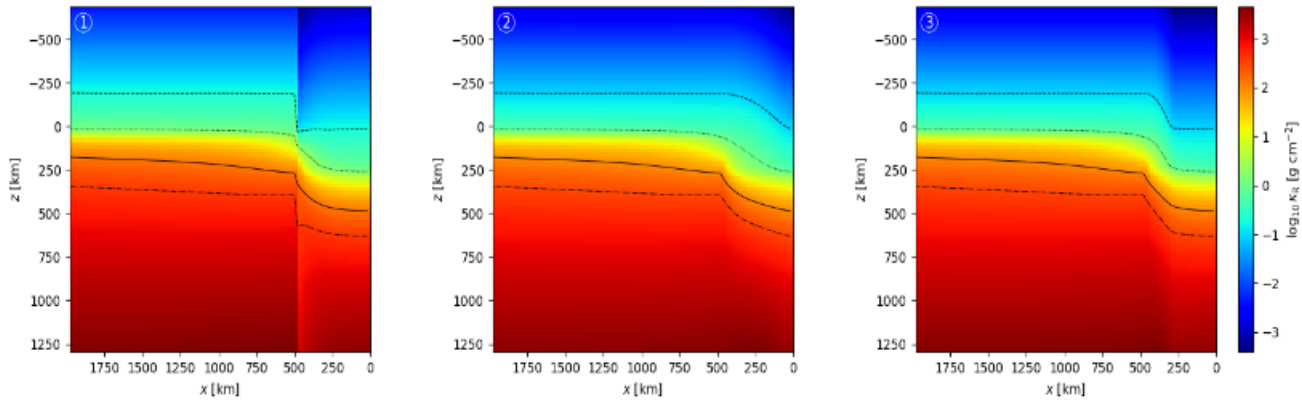

Figure 27: *Opacity distribution with different treatment for the transition zone. From left to right: variants 1, 2, 3 of p_0, see Figure 10. Isobars at 10^{-1} (dashed line), 10^0 (dotted line), 10^2 (solid line), $10^{2.5}$ (dash-dotted line) g* cm^{-2}.

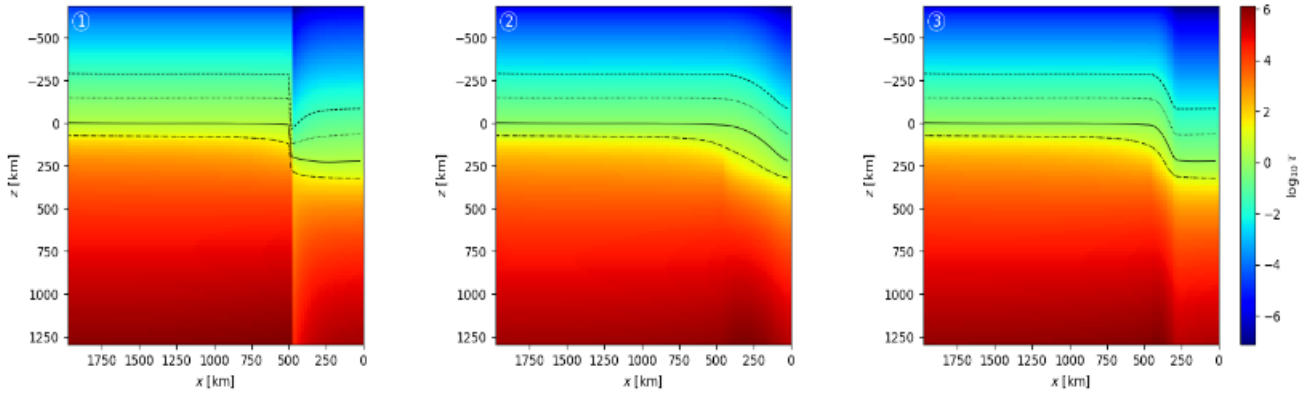

Figure 28: *Optical depth distribution with different treatment for the transition zone. From left to right: variants 1, 2, 3 of p_0, see Figure 10. Isobars at 10^{-2} (dashed line), 10^{-1} (dotted line), 10^{0} (solid line), 10^{1} (dash-dotted line).*

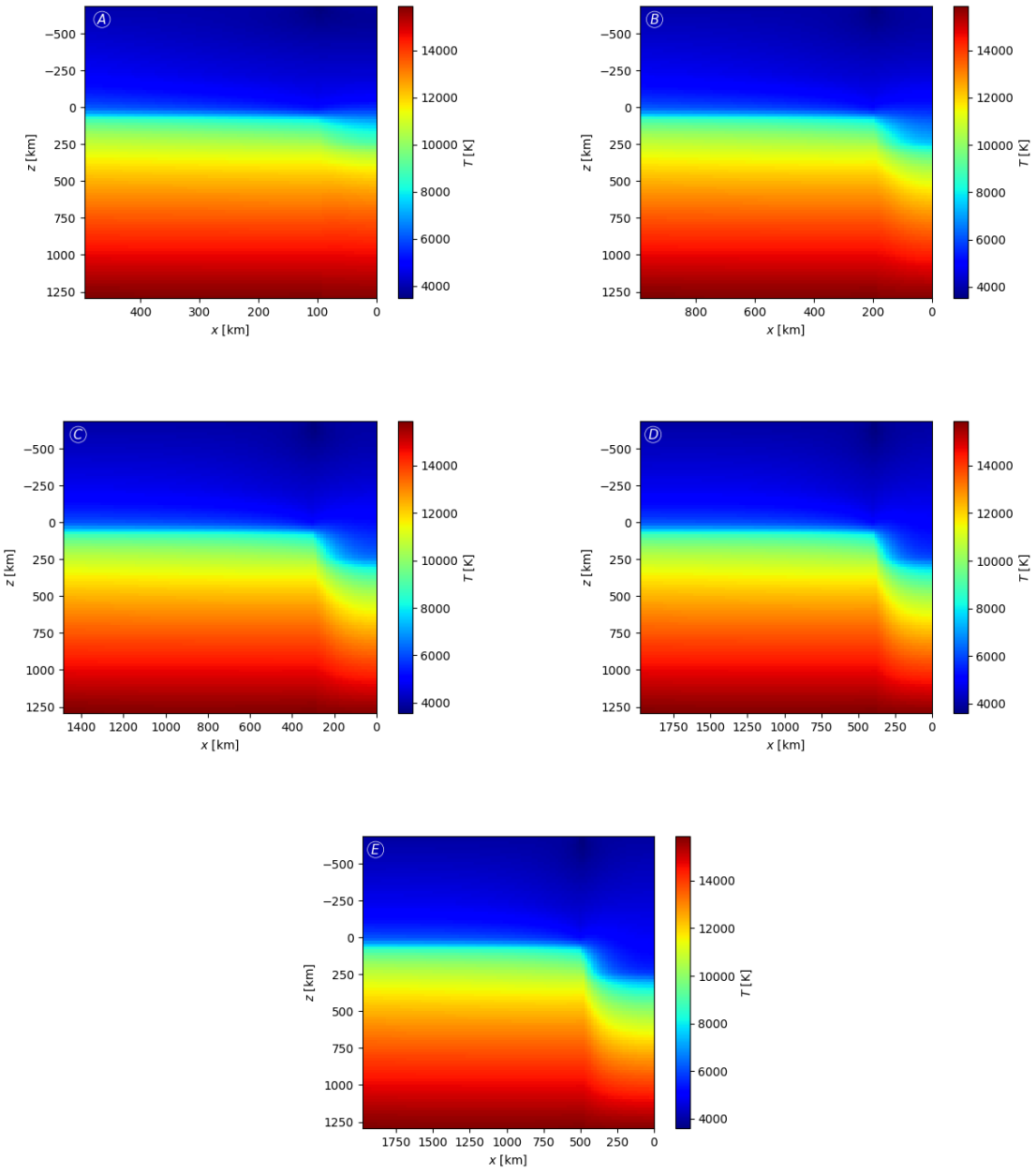

Figure 29: *Temperature distribution of models A-E. (Table 2)*

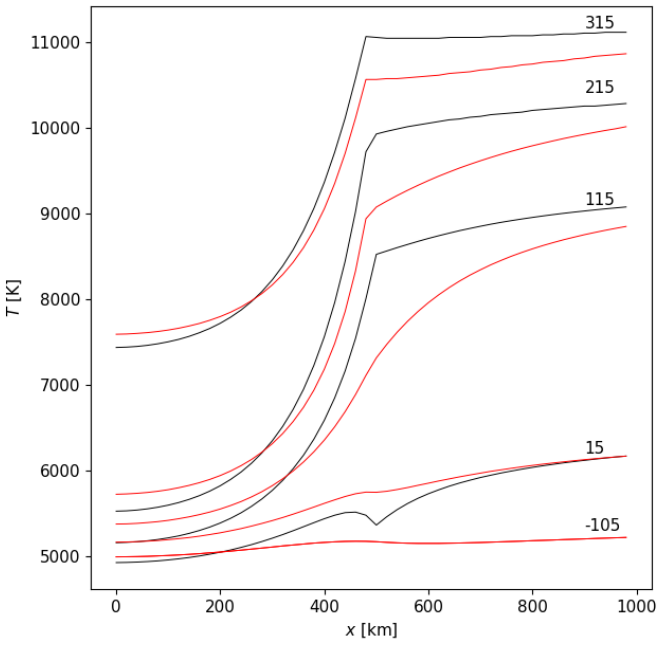

Figure 30: *Temperature at several depths (indicated at the curves, in km), black line for model E (Table 2) and red line for the same model without ΔT method.*

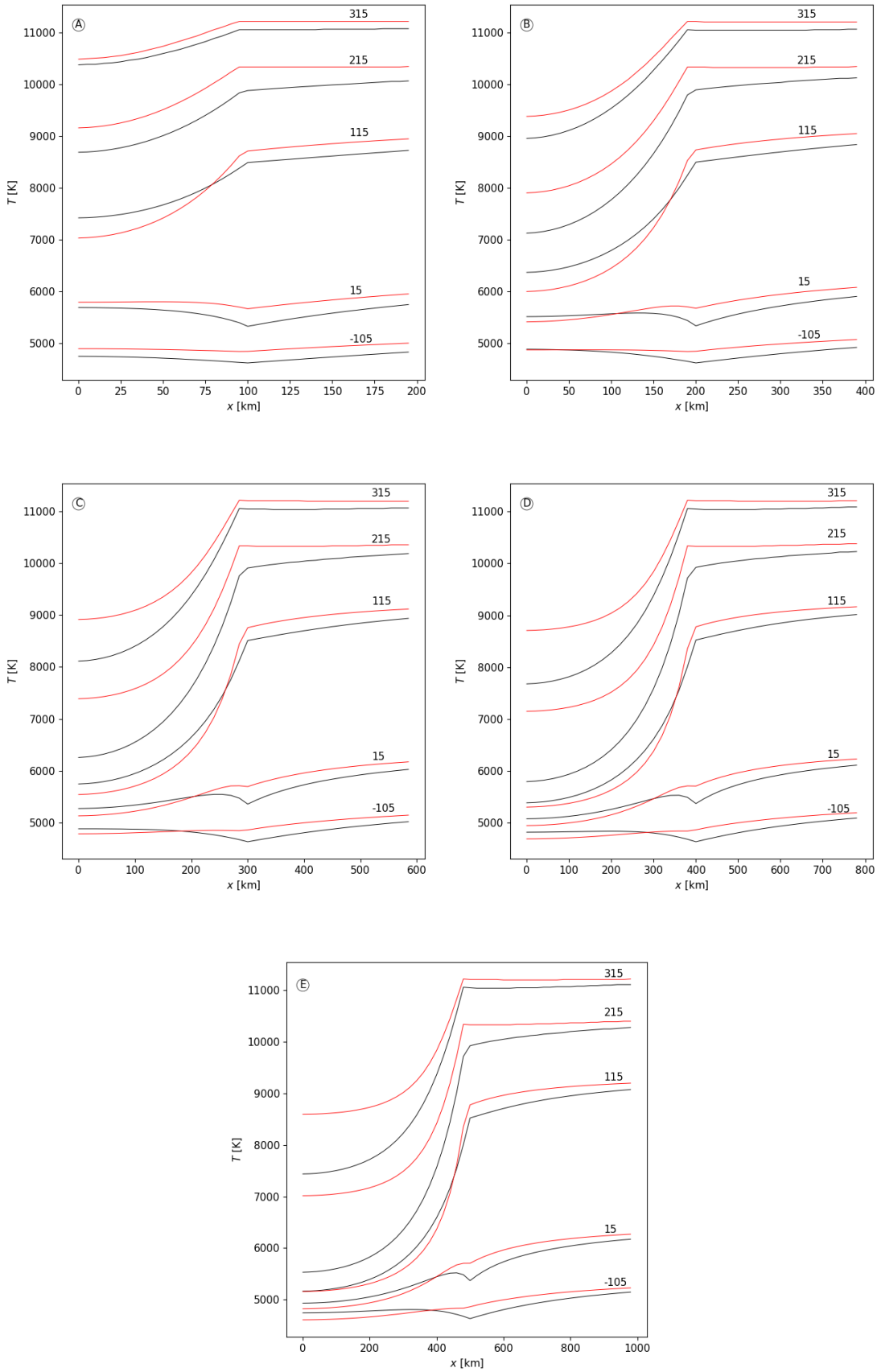

Figure 31: *Temperature at several depths (indicated at the curves, in km), for models A-E (black line), red line represent the same models modifying $z_w = 100$ km, models A*-E* (Table 2).*

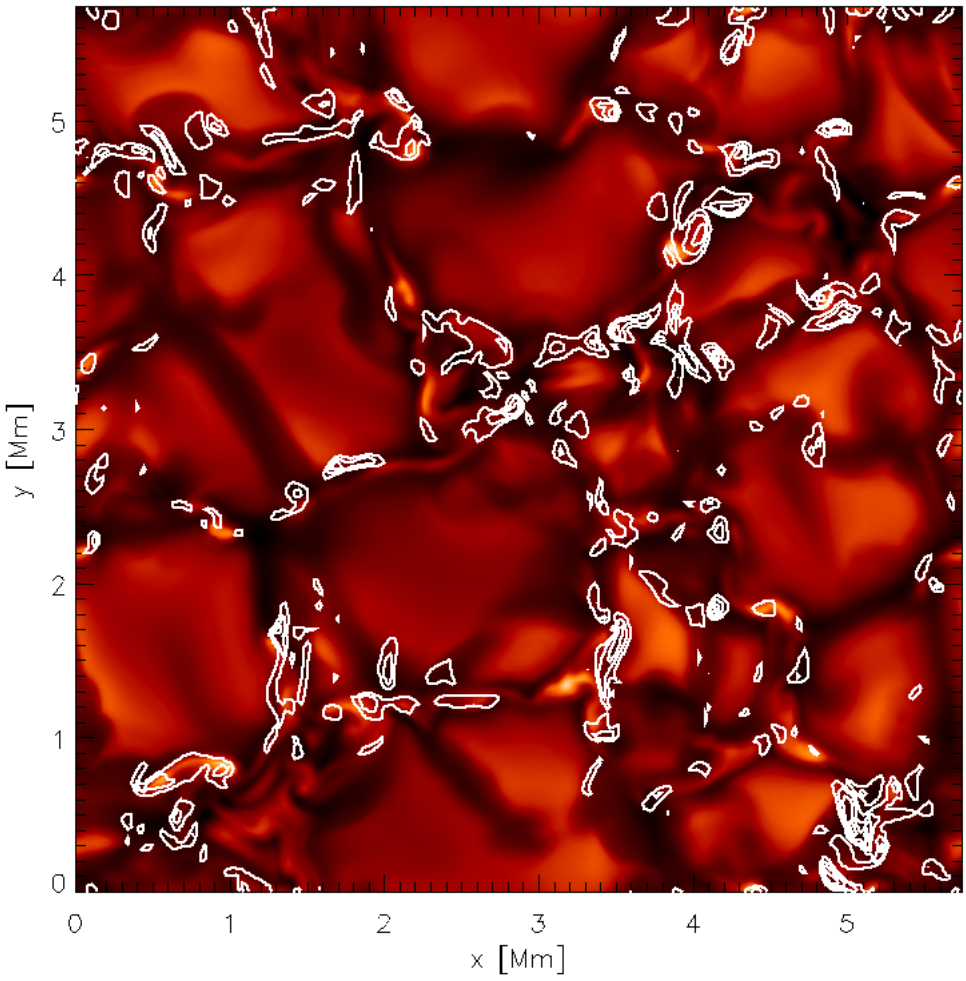

Figure 32: *Specific intensity computed from a simulation of solar near-surface convection with vertical field of 200 G (Vitas et al., 2009). The white contour show the concentration of the vertical magnetic field at the geometrical height 210 km below the height of the mean optical depth unity.*

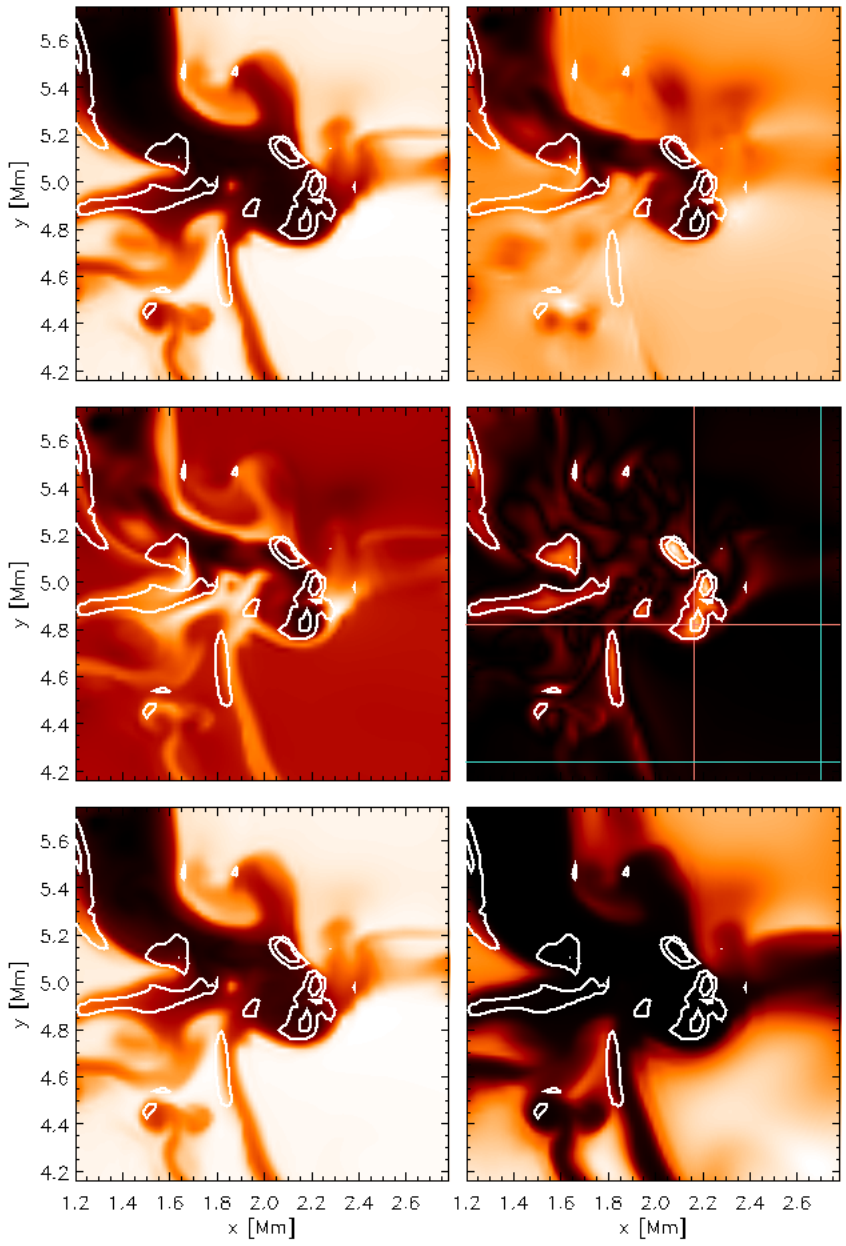

Figure 33: *The horizontal sections through the simulation cube described in the text at the geometrical level 200 km below the mean surface. Top row: the temperature and the gas pressure; middle row: the mass density and the vertical magnetic field; bottom row: the continuum opacity and the optical depth. As we are interested only in the qualitative description, we omit the color-bars from this figure. The white contours show the magnetic field at this geometrical height. The cross-lines indicate typical pixels, one representing the axis of a magnetic element (red) and one representing the quiet photosphere (blue).*

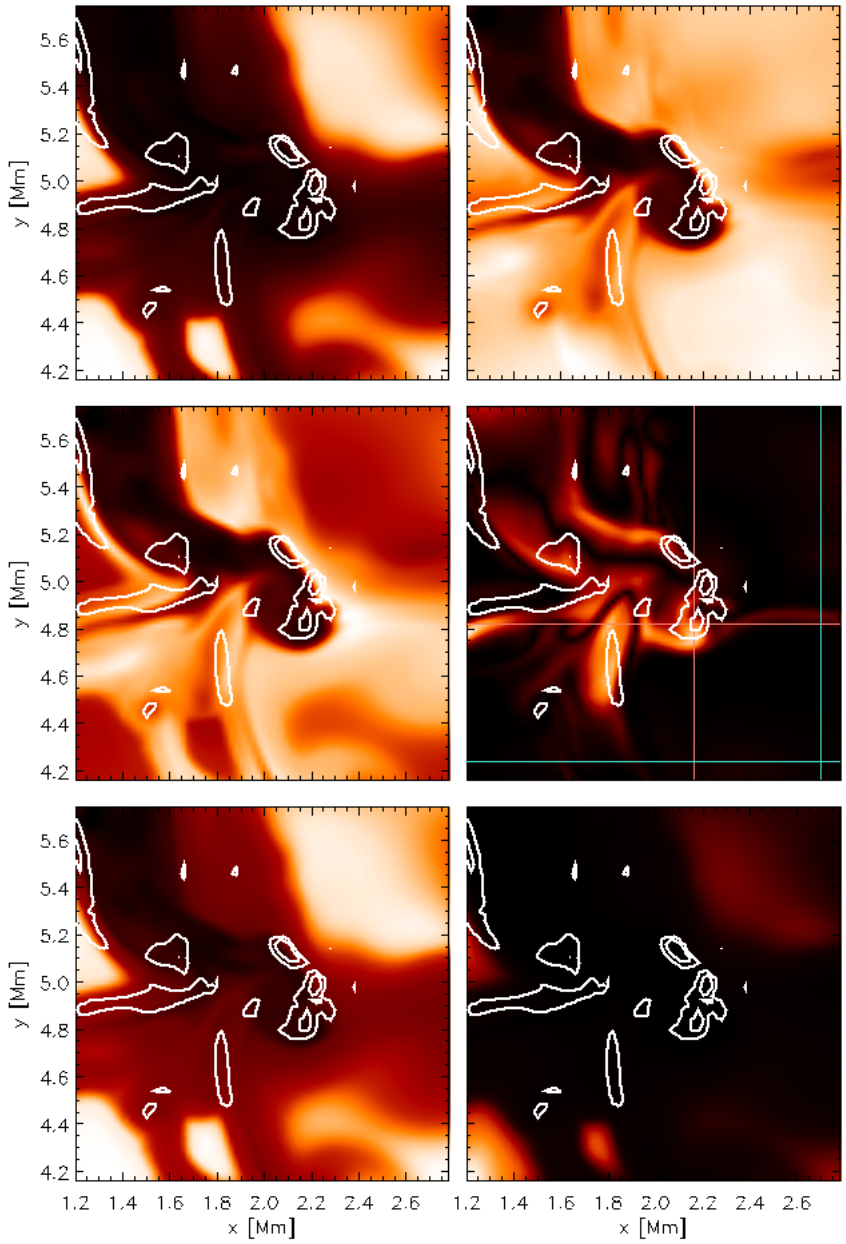

Figure 34: *Same as Fig. 33, but the sections are taken at geometrical height corresponding to the mean surface.*

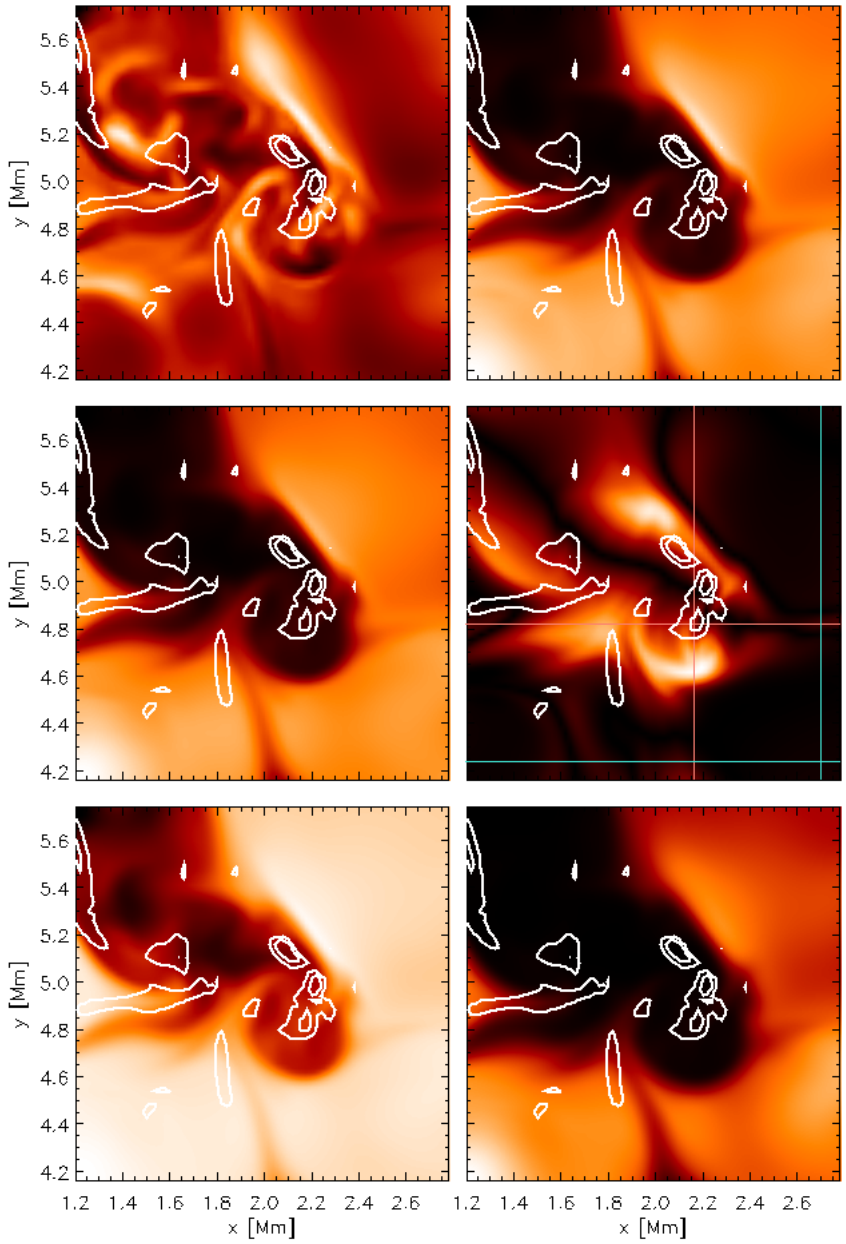

Figure 35: *Same as Fig. 33, but the sections are taken at geometrical height 280 km above the mean surface.*

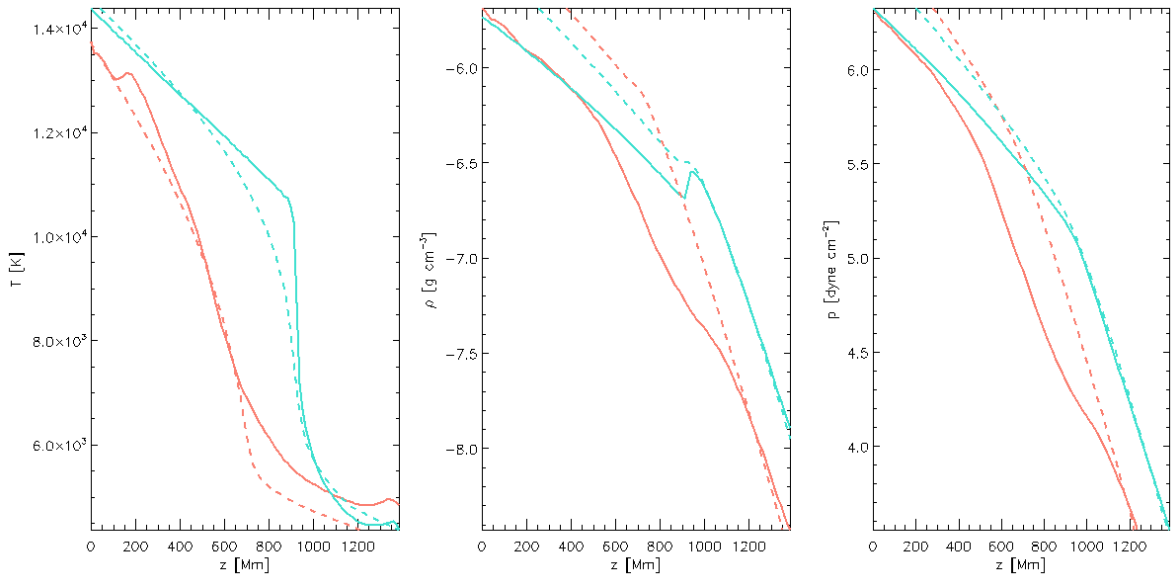

Figure 36: *The vertical stratification of T (left), $\log \rho$ (middle) and $\log p$ (right). The data corresponding to the magnetic element is in red, to the photosphere in blue. The data from the 3D simulation is shown in solid curves, and from our model in dashed.*

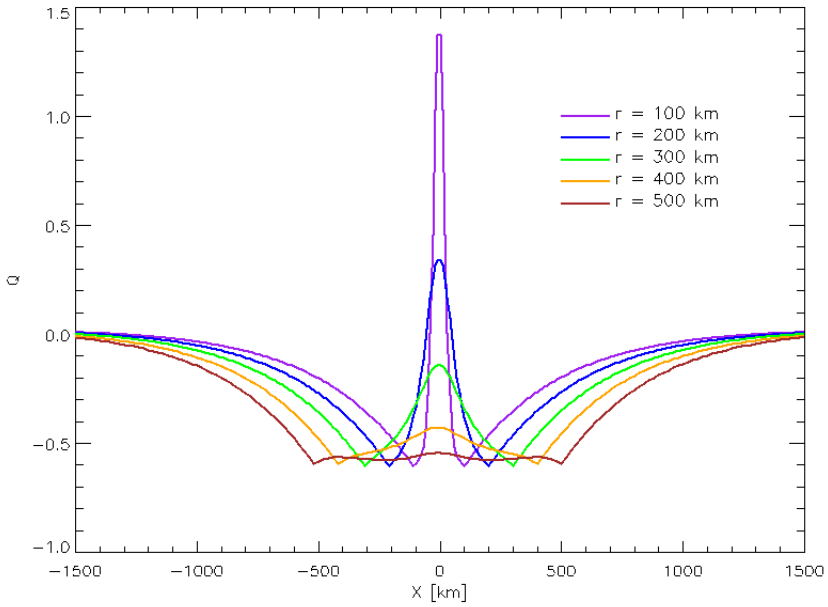

Figure 37: *The dimensionless contrast of the specific intensity Q at 500 nm, against the horizontal axis in our models A to E.*

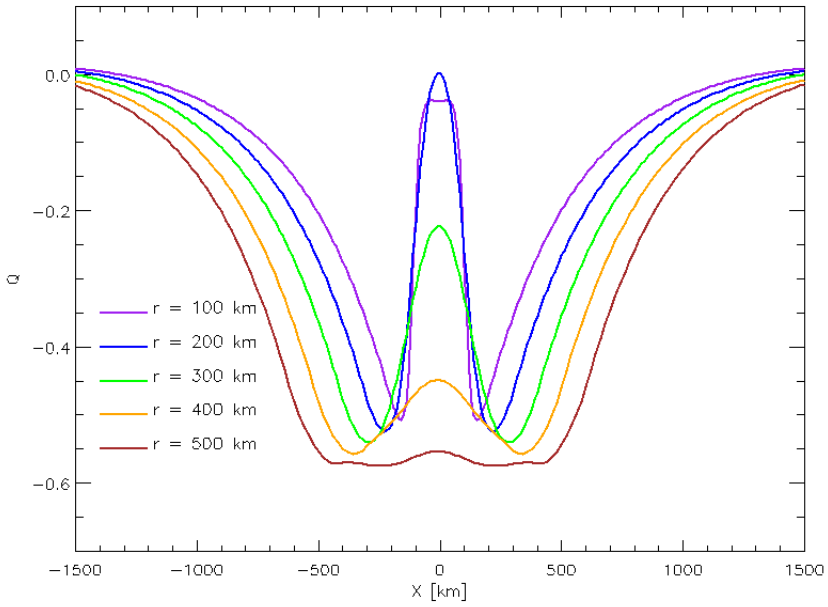

Figure 38: *Same as Fig. 37, but the profiles are convolved with a Gaussian with FWHM of 200 km.*